A Preliminary Evaluation of GOES-16 Active Fire Product using Landsat-8 and VIIRS Active Fire Data, and Ground-based Prescribed Fire Records

Fangjun Li[a]*, Xiaoyang Zhang[a], Shobha Kondragunta[b], Christopher C. Schmidt[c], and Christopher D. Holmes[d]

[a] Geospatial Sciences Center of Excellence, department of Geography, South Dakota State University, Brookings, SD 57007, USA

[b] NOAA/NESDIS/Center for Satellite Applications and Research, College Park, MD 20740, USA

[c] Cooperative Institute for Meteorological Satellite Studies (CIMSS), University of Wisconsin-Madison, Madison, WI 53706, USA

[d] Department of Earth, Ocean and Atmospheric Science, Florida State University, Tallahassee, FL 32306, USA

*Corresponding author: Fangjun Li (fangjun.li@sdstate.edu)

Abstract

Satellite-based active fire data provide indispensable information for monitoring global fire activity and understanding its impacts on climate and air quality. Yet the limited spatiotemporal sampling capacities of current satellites result in considerable uncertainties in fire observation and emissions estimation. The mitigation of these uncertainties mainly relies on new remote-sensing technology. The Advanced Baseline Imager (ABI) onboard the Geostationary Operational Environmental Satellite-R (GOES-R) Series observes fires across North and South Americas at an unprecedentedly spatiotemporal resolution of nominal 2 km every 5-15 minutes. This study evaluated the GOES-16 (the first GOES-R satellite) ABI active fire product using active fire data derived from the 30-m Landsat-8 and the 375-m and 750-m Visible Infrared Imaging Radiometer Suite (VIIRS), and ground-based burning data across the southeastern Conterminous United States (CONUS) during the 2018 peak fire season. Specifically, we characterized the overall fire detection performance of the ABI active fire detections, estimated omission and commission errors, and evaluated ABI fire radiative power (FRP). The results showed that the ABI fire detection probability and its omission and commission errors were highly related to fire size and temporal period. ABI detection probability was higher than 95% for the fire pixel that contained over 114 Landsat-8 (30 m) fire detections or 11 VIIRS (375 m) detections. During a period of ±8 hour, ABI detected 19% and 29% more fires observed by Landsat-8 and 375-m VIIRS, respectively. Correspondingly, the omission error could reduce by up to 33%. Further, ABI was able to detect 6-22% and 31-42% more ground-recorded fires than VIIRS in Georgia and Florida States, respectively, but ABI still missed many very small fires because ABI was hard to detect fires smaller than ~34.5 MW. Additionally, compared with 750-

m VIIRS FRP, ABI FRP was ~30-50% larger in individual fire events but was overall similar at a regional scale.

Keywords

GOES-16; Landsat8; VIIRS; Active Fire Product Evaluation; Southeastern CONUS

1 Introduction

Biomass burning contributes substantially to atmospheric greenhouse gases and aerosol emissions that significantly influence climate (Jacobson, 2014), degrade regional air quality (Liu et al., 2018; Marlier al., 2015), and threaten public health (Huff et al., 2015; Johnston et al., 2012). The satellite-based fire data provide a great tool to monitor regional-to-global biomass burning. For example, burned area and active fire data from polar-orbiting and geostationary satellites were widely used to investigate the spatial distribution (Giglio et al., 2006), diurnal and weekly cycles (Earl et al., 2015; Giglio, 2007; Roberts et al., 2009; Zhang et al., 2012), and seasonal and annual variations of global fire activity (Andela et al., 2017; Earl and Simmonds, 2018; Zhang et al., 2014). More importantly, the satellite-based fire data also provide estimates of area burned and fire-released radiative energy that were extensively applied to generate biomass-burning emissions products for a long term period (Ichoku and Ellison, 2014; Li et al., 2019; van der Werf et al., 2017) and in near-real time (Darmenov and Silva, 2015; Kaiser et al., 2012; Zhang et al., 2012). These emissions products provide one of essential inputs for atmospheric transport models to forecast air quality (Reid et al., 2009; Wang et al., 2018; Wiedinmyer et al., 2006; Yang et al., 2011). Yet the capacities of these models are limited by high uncertainties in emissions estimates. For the emissions estimates that based on satellite active fire data, the associated uncertainty is mainly due to relatively poor temporal and spatial resolutions of current satellites (Ichoku et al., 2012; Freeborn et al., 2011).

Mitigation of uncertainties in biomass-burning emissions estimates counts on the advancement of new satellite sensors. Particularly, the Advanced Baseline Imager (ABI) onboard the new generation of Geostationary Operational Environmental Satellite-R (GOES-R) Series detects fires at an unprecedented spatiotemporal resolution of nominal 2 km at nadir every 5-15 min over North and South Americas (up to 1 min in super-scan mode in subregions) (Schmit et al., 2017). GOES-16, the first satellite of GOES-R series, which was launched on November 2016, has been running in an operational mode at 75°W longitude above the equator and providing active fire detection data since late December 2017 (Schmit et al., 2017). Following GOES-16 is another identical satellite, GOES-17, which was launched on March 1, 2018 and positions at 137°W longitude above the equator for operational running since February 12, 2019. Then, GOES-16 and 17 will observe fires across Americas from east and west, respectively. Likewise, the 2-km Advanced Himawari Imager (AHI) onboard Himawari-8/9 satellites observes fires over Southeast Asia and Australia every 10 min (Xu et al., 2017) and the 3-km Spinning Enhanced Visible and Infrared Imager (SEVIRI) onboard Meteosat satellites (MSG) senses Africa, Europe, and a part of South America every 15 min (Roberts et al., 2005).

This study is for the first time to assess the fire detection and characterization capability of the GOES-16 ABI sensor in the southeastern Conterminous United States (CONUS). In the southeastern CONUS, prescribed fires account for ~70% of national burned acreage by prescribed fires per year (Melvin, 2015), which could contribute ~27% of the air pollutant PM2.5 (particulate matter with a diameter of less than 2.5 micrometers) during peak burning season from January to April, although all prescribed burnings should follow state-level and/or local air quality policies (Tian et al., 2008; Zeng et al., 2008; Zhang et al., 2010). Compared with the western CONUS forest wildfires that could generally burn very large areas and last several months due to climate change and fire suppression efforts (Abatzoglou et al., 2016; Littell et al., 2009; Minnich, 1983), fires in the southeastern CONUS are primarily small-sized prescribed fires that burn in relatively lower intensity in agriculture and forestry lands (Fowler and Konopik, 2007). Thus, it is relatively challenging to detect and map the prescribed burnings in the southeastern CONUS (Randerson et al., 2012) where the annual burned areas from satellite-based products were underestimated by a factor of 3-4 (Huang et al., 2018; Nowell et al., 2018). The new GOES16 ABI sensor is expected to provide a good opportunity to improve fire detections in this region.

Active fire detections from a coarser resolution satellite data have been commonly evaluated using finer resolution data. For example, the 30-m Advanced Spaceborne Thermal Emission and Reflection Radiometer (ASTER) onboard the NASA Terra satellite was successfully used to detect active fires to validate fire detections from MODerate resolution Imaging Spectroradiometer (MODIS) and previous GOES (Morisette et al., 2005a, 2005b; Csiszar et al., 2006; Schroeder et al., 2008; Giglio et al., 2008). Due to the dysfunction of the ASTER shortwave infrared (SWIR) bands since 2008, the 30-m Landsat-7 Enhanced Thematic Mapper Plus (ETM+) and Landsat-8 Operational Land Imager (OLI) have been used to detect fires at 30 meter (Kumar and Roy, 2018; Murphy et al., 2016; Schroeder et al., 2008, 2016). Thus, the Landsat active fire data become the major data source for evaluating and validating fire detections from coarser sensors. Because of inability of the Landsat active fire data to provide fire radiative power (FRP), evaluation of FRP from coarse sensors, like geostationary sensors (e.g., SEVIRI and AHI), mainly relies on the 1-km MODIS FRP (Roberts and Wooster, 2008; Roberts et al., 2015; Xu et al., 2017). The FRP evaluation could be improved using the sub-kilometer FRP from the latest moderate-resolution sensor – the Visible Infrared Imaging Radiometer Suite (VIIRS) onboard the Suomi National Polar-orbiting Partnership (S-NPP) and NOAA-20 satellites as it is able to detect more small fires than MODIS (Csiszar et al., 2014; Schroeder et al., 2014).

Therefore, the new GOES-16 ABI senor's fire detection and characterization capability is evaluated in this study using the 30-m Landsat-8, 375-m and 750-m S-NPP VIIRS active fire data, and ground-based burning records as reference data. Specifically, the evaluation is conducted in the following steps. First, we modeled the fire detection performance of the GOES-16 ABI sensor using logistical regression models using contemporaneous 30-m Landsat8 and 375-m VIIRS active fire data. Second, the omission and commission errors of ABI active fire data were investigated by referencing the 30-m Landsat8 and 375-m VIIRS active fire data. Third, the GOES-16 ABI fire detection capability was further evaluated by comparing with the ground-based records of prescribed fires. Finally, we evaluated GOES-16 ABI fire radiative power (FRP) by comparing with the contemporaneous 750-m VIIRS active fire data in individual fire events and at regional scales.

2 Data

2.1. GOES-16 ABI Active Fire Data

GOES-16 ABI operationally observes fires across the CONUS every 5 min with a view zenith angle (VZA) of about 29°-72°. The ABI active fire product detects and characterizes actively burning fires mainly based on the 3.9-µm and 11.2-µm bands using a contextual fire detection algorithm that is built on the WildFire Automated Biomass Burning Algorithm (WF_ABBA) (Schmidt et al., 2012). The WF_ABBA algorithm was developed for the legacy GOES satellites and has been running operationally since the beginning of 21th century (Prins and Menzel, 1994; Schmidt and Prins, 2003). The ABI active fire product characterizes each fire detection using the parameters of detection time, fire area, fire temperature, FRP (MW/pixel), and fire mask code (Schmidt et al., 2012). The fire area and temperature parameters are estimated at a subpixel level using a modified Dozier method (Dozier, 1981). The FRP is estimated from the radiances of a fire pixel and its ambient background non-fire pixels on the 3.9-µm band using the method proposed by Wooster et al. (2003) defined as:

$$FRP = \left(\frac{A\sigma}{\alpha} \qquad {}_{,MIR} - \quad {}_{B,MIR}\right) \tag{1}$$

where, for an ABI fire pixel, *FRP* is fire radiative power (units: MW); *A* is pixel area (units: km^2); σ is the Stefan–Boltzmann constant (σ=5.67×10^{-8} Wm^{-2} K^{-4}); α is a sensor-specific constant (α=3.0×10^{-9} Wm^{-2} sr^{-1} µm^{-1} K^{-4} for the ABI sensor, Schmidt et al., 2012). $L_{f,\ MIR}$ and $L_{B,\ MIR}$ are radiances of the fire pixel and its ambient background non-fire pixels on the ABI middle-infrared band (3.7 - 4.1µm with a center wavelength of 3.9µm, Fig. 1). The fire mask code classifies the ABI fire pixel into six categories (processed, saturated, cloud contaminated, high possibility, medium probability, and low probability) (Schmidt et al., 2012). The GOES-16 ABI 3.9-µm band has a saturation temperature of 400K that largely reduces the number of saturated fire pixels compared to the legacy GOES (Schmidt et al., 2012). Similar to the previous WF_ABBA algorithm (i.e., V65), the ABI fire algorithm for each fire detection also applies a temporal filter to reduce false alarms by considering fire detection information before and after the fire detection (Schmidt et al., 2012). The temporal filter flags an ABI fire as a temporally filtered pixel if a previous fire detection was sensed within one ABI pixel distance of this fire pixel in the past 12 hours (Schmidt et al., 2012). Thus, the ABI active fire product provides both unfiltered and temporally filtered fire detections that are flagged using different codes in ABI fire mask.

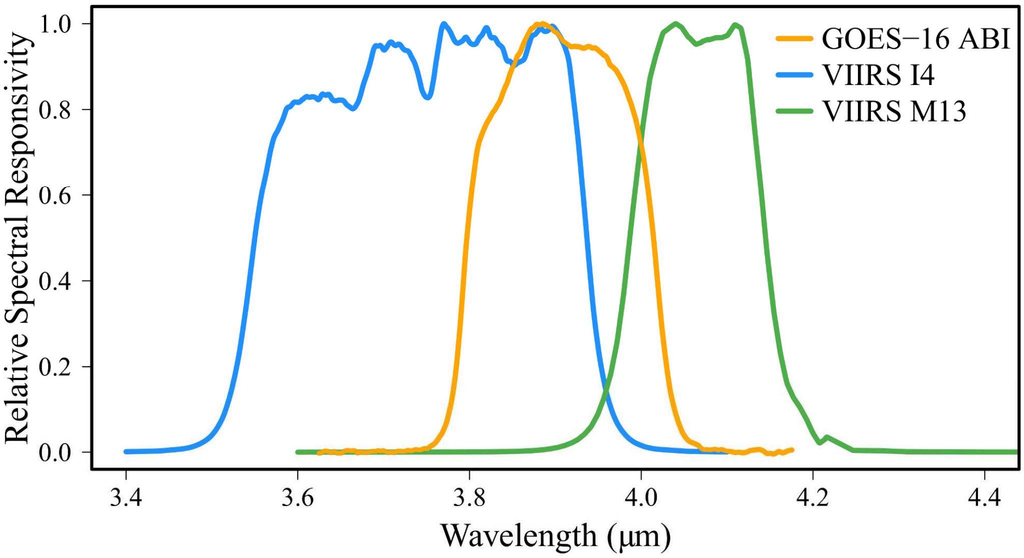

Fig. 1. Relative spectral response functions of the fire-detecting middle-infrared bands of GOES-16 ABI (channel7 at ~3.71-4.09µm) and Suomi NPP VIIRS (I4 at ~3.47-4.03µm and M13 at ~3.89-4.24µm). The ABI and VIIRS relative spectral response functions were obtained from NOAA National Calibration Center (https://ncc.nesdis.noaa.gov/index.php).

The 2-km ABI active fire product, currently at "provisional" status, is an ABI Level2 product that is defined using the ABI fixed grid projection. It consists of 1500 (south-to-north direction) by 2500 (east-to-west direction) pixels over the CONUS with a horizontal spatial resolution of 56 microradian (µrad) in view angle (2 km at nadir) in both directions (*Carlomusto*, 2018). The fire pixel area increases from ~4.8 to ~6.2 km^2 as the ABI VZA increases from 29° to 45° in the southeastern CONUS (Fig. 2). Therefore, the fire pixel geometry is generally consistent across the region. The geolocation (geodetic longitude and latitude) for the center of an ABI fire pixel can be calculated from the ABI view geometry (i.e., elevation angle and scanning angle) and the horizontal spatial resolution (56 μrad) (Carlomusto, 2018).

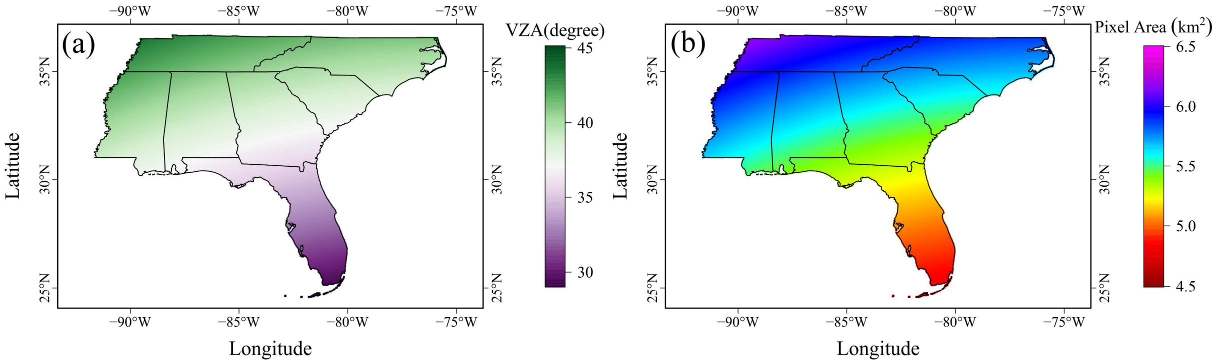

Fig. 2. GOES-16 ABI view zenith angle (a) and pixel area (b) across the southeastern CONUS.

This study used near four months of the ABI 2-km Level-2 active fire data from 24 January to 30 April 2018 based on the following two reasons. First, the ABI sensor was not switched to operation mode until late December 2017. Although the ABI active fire data were produced for the period when ABI was in test mode, the ABI fire data after operational running represent better quality of fire detections. Second, the four months from January to April are the peak-burning season in the southeastern CONUS (Giglio et al., 2006; Nowell et al., 2018; Zhang et al., 2014), which provides the best opportunity to evaluate ABI's fire detection and characterization capability in this region. Thus, we obtained both the filtered and unfiltered ABI active fire data from the Cooperative Institute for Meteorological Satellite Studies in University of Wisconsin–Madison where the ABI active fire algorithm was developed. Among all the fire detections during the period, percentages of the six-category ABI fire detections are 35% of processed, less than 0.1% of saturated, 8.5% of cloud contaminated, 4.5% of high possibility, 4% of moderate possibility, and ~48% of low possibility, respectively.

2.2. Landsat-8 Active Fire Data

Although there is no designed band for fire detection, the 30-m visible and near infrared (VNIR) and SWIR bands of the Landsat-8 Operational Land Imager (OLI) have been successfully used to detect thermal anomalies (i.e., actively burning fires) (Kumar and Roy, 2018; Murphy et a., 2016; Schroeder et al., 2016). From OLI VNIR and SWIR bands collected every 16 days, active fires have been detected using three algorithms (Kumar and Roy, 2018; Murphy et al., 2016; Schroeder et al., 2016). The fire detection performances of these algorithms were empirically evaluated by comparing with the Google Earth imageries visually, some simulated fires, and a very limited number of ground observations (Kumar and Roy, 2018; Schroeder et al., 2016). The evaluation results showed that none of the three algorithms consistently outperforms the others in the regions with distinct fire characterizations (Kumar and Roy, 2018; Murphy et al., 2016). However, the algorithm proposed by Schroeder et al. (2016) was implemented to routinely produce 30 m Landsat active fire data for the United States fire management community at the USDA (United States Department of Agriculture) Remote Sensing Applications Center.

This study used the Landsat-8 active fire data detected from the Schroeder's algorithm that has an overall good performance with commission errors less than 0.2% globally (Schroeder et al., 2016). The Landsat-8 active fire data were obtained from USDA Remote Sensing

Applications Center (https://fsapps.nwcg.gov/afm/gisdata.php) in the southeastern CONUS for the study period from January to April 2018. However, we noticed that this dataset missed fire detections from Landsat-8 scenes that were not processed for many significant burning days. To collect enough active fire samples, we implemented the Schroeder's algorithm for additional 92 Landsat-8 daytime scenes that were collected for 20 significant burning days under cloud-free conditions from January to April 2018. To ensure that our implementation produces consistent active fire data with the USDA product, we applied the Schroeder's algorithm to another 10 Landsat-8 daytime scenes that were processed by USDA and compared the two fire detection results. The comparison results showed a difference as low as less than 4%, which means that more than 96% of fire detections were identical between USDA and our implementations. Thus, we are confident of using both the Landsat-8 active fire data together with negligible effects on our analyses. As a result, the Landsat-8 active detections increased by about 130% after adding the 92 scenes (Fig. 3). Note that the Landsat-8 OLI scene data (Landsat-8 L1T product) used in this study were obtained from the United States Geology Survey (USGS) data port "EarthExplore" (https://earthexplorer.usgs.gov/).

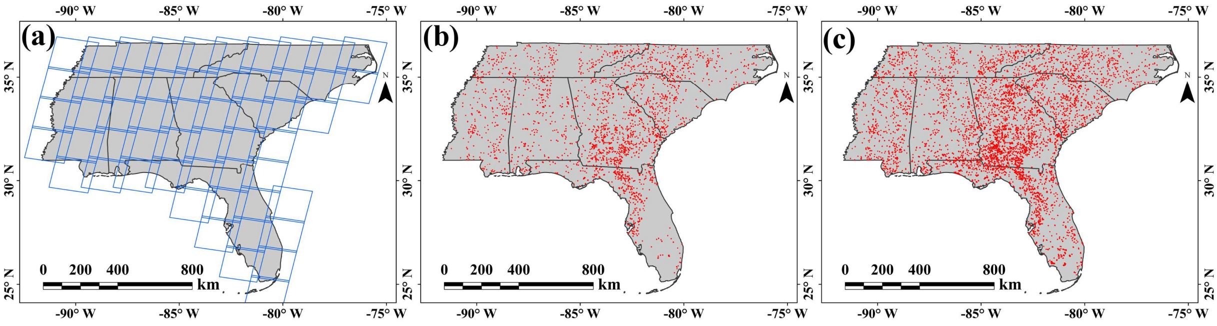

Fig. 3. Distributions of 56 Landsat-8 scenes (a) and active fire detections across the southeastern CONUS between January and April 2018 from USDA (b) and from both USDA and this study (additional 92 scenes) (c).

2.3. VIIRS Active Fire Data

We obtained the 375-m S-NPP VIIRS Level2 active fire product (named VNP14IMG) from the NASA Level-1 and Atmosphere Archive & Distribution System (LAADS, https://ladsweb.modaps.eosdis.nasa.gov/archive/allData/5000/VNP14IMG/). The VNP14IMG for the first time provides daily active fire data globally at a sub-kilometer resolution. The product contains for each fire pixel the detection time, geolocation, detection confidence (low, nominal, and high), FRP, brightness temperatures at the 4-μm and 11-μm imagery bands (I-bands), satellite view zenith, and solar zenith angles (Schroeder et al., 2014; Schroeder and Giglio, 2017). The VIIRS 4-μm I-band (I4 at 3.47-4.03μm, Fig. 1) has a 367 K saturation temperature, which could be easily saturated for intense fires and is very challenging for FRP characterization (Schroeder et al., 2014). Therefore, the FRP recorded in the 375-m VNP14IMG product is indirectly derived from the radiances of the collocated 750-m pixel and background non-fire pixels at the 4-μm Moderate-resolution band (M-band13, or M13, at 3.89-4.24μm) that has a high saturation temperature of ~634K (Schroeder et al., 2014; Schroeder and Giglio, 2017).

We also obtained the S-NPP VIIRS 750-m NDEAF-L2 active fire products from the NOAA Comprehensive Large Array-Data Stewardship System (CLASS) (https://www.class.ncdc.noaa.gov/). The NDEAF-L2 represents S-NPP Near-real-time Data Exploitation Level-2 Active Fire, which is generated using a modified MODIS Collection 6 (C6) active fire detection algorithm (Giglio et al., 2016a, 2016b), and provides for each fire pixel similar fire information to the 375-m VIIRS VNP14IMG active fire product (Csiszar et al., 2016; Schroeder and Giglio, 2017). The detection confidence that ranges from 0-100% is further grouped into three categories (low, nominal, and high) (Giglio et al., 2003, 2016a). A preliminary assessment shows that NDEAF-L2 is globally comparable with the MODIS C6 active fire product (Li et al., 2018). Note that a similar 750-m VIIRS Level-2 active fire product is also produced based on the same fire detection algorithm as that of NDEAF-L2 product in NASA, which is named as VNP14 (Schroeder and Giglio, 2017). Thus, the two products are the same essentially. There are two reasons why we chose the NOAA NDEAF-L2 product in this study. First, the NOAA VIIRS NDEAF-L2 product is an operational product that provides one of key inputs in a near-real time manner for many applications (e.g., modeling transportation of smoke aerosols (Ahmadov et al., 2017) and producing daily global biomass-burning emissions (Zhang et al., 2017b)). Second, we have evaluated FRP from this product by comparing it with MODIS FRP (Li et al., 2018). The evaluation results suggest that VIIRS FRP is generally comparable with MODIS FRP in individual fire events but it is slightly larger at a continental scale because the 750-m VIIRS M-band has higher capability of detecting relatively small and/or cool fires than the 1-km MODIS (Li et al., 2018).

Moreover, the VIIRS Moderate Bands Terrain Corrected Geolocation (GMTCO) product was obtained from the NOAA CLASS for the same period. The VIIRS GMTCO product was used to build the VIIRS granule boundaries for extracting the contemporaneous GOES-16 ABI fire detections and was applied to correct the duplicate fire detections between VIIRS adjacent scans at off-nadir view angles following the method in Li et al. (2018).

2.4. Ground Records of Prescribed Fires

This study used ground records of prescribed fires in Georgia and Florida States. The Georgia Forestry Commission (GFC) and the Florida Forest Service (FFS) agencies separately manage a database of long-term statewide prescribed-burning permits records and provide us the ground fire records for the period from January to April 2018. In Georgia State, the GFC issues three-type burning permits that are burnings to clean small yard debris, burnings in an air curtain destructor (a small-size tool used to burn wood waste), and burnings of at least one acre (~0.004 km^2) in size (named acreage burn permits). Each record of acreage burn permits includes permit number, burning date, start and end times, geolocation (if provided), approximate size planned to burn, and approval status (approved/denied). Because the size was very small for the first two-type burnings, this study only used the officially approved acreage burn permits that were for agricultural, silvicultural, or land clearing purposes, by which geolocations (longitude and latitude) were generally required for burns over 100 acres (~0.404 km^2) although they could be also provided for burns less than 100 acres by permit applicants. As a result, a total of 3133 acreage burn permits in Georgia State were used, which were summarized in Table 1. However, the acreage burn permit does not clearly specify burning purpose (i.e., agricultural, silvicultural, or land clearing).

In Florida, the FFS issues burn permits for agricultural, silvicultural, land clearing, and pile burnings. Each permit record provides burning information including permit number, burning date, burning type, geolocation, and approximate size planned to burn. Comparing with burn permits in Georgia, each burn permit in Florida clearly specifies its burning purpose but does not include start and end burning times. The first three burn types have a size of at least one acre. However, pile burnings can be very small as they are generally used to clear debris and the associated burn permits record no information on acres to burn. Thus, pile burn permit records were not included in analysis. As a result, a total of 2903 burn permits in Florida were used (Table 1).

Table 1. Approved burn permits in Georgia and Florida States in the selected days.

State	Burn Purpose	Number of Permit	Acres to be Burned (acres)			
			Min	Max	Mean	Standard Deviation
Georgia	All	3133	1	2206	96.0	155.1
Florida	Silvicultural	1396	1	20000	212.4	718.5
	Agricultural	1487	1	40000	77.9	1041.2
	Land Clearing	20	1	200	39.0	60.1
	All	2903	1	40000	142.3	898.8

3 Methods

3.1. Modeling the Fire Detection Probability of the GOES-16 ABI

Fire detection probability characterizes the performance of the associated fire detection algorithm and provides important information for future algorithm improvement (Csiszar et al., 2006). In the validation process of the 1-km MODIS active fire product, previous studies applied logistical regression models to estimate the fire detection probability of the MODIS sensor by comparing with the contemporaneously collocated 30-m ASTER fire pixels in Southern Africa, Northern Eurasia, and Brazilian Amazonia (Morisette et al., 2005a; Csiszar et al., 2006; Schroeder et al., 2008). By using a similar approach, we modeled the fire detection probability of the 2-km ABI sensor using the contemporaneously collocated 30-m Landsat-8 and 375-m S-NPP VIIRS active fire detections based on the following steps (Fig. 4).

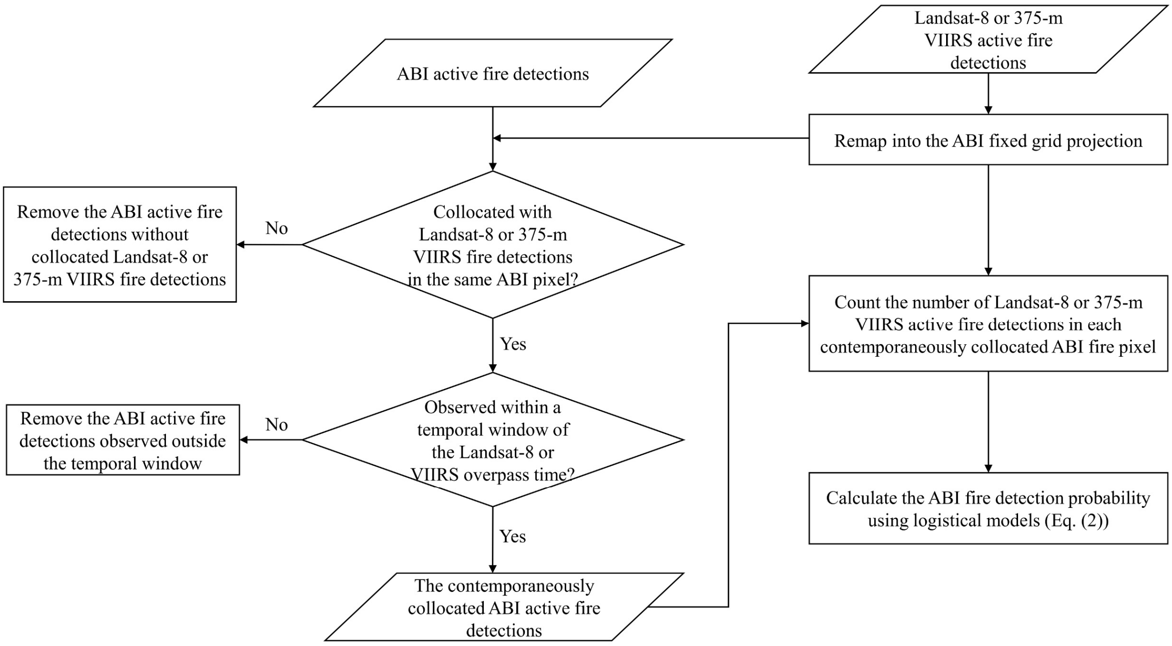

Fig. 4. Flowchart of modeling the ABI fire detection probability using the contemporaneous Landsat-8 and 375-m VIIRS active fire detections.

First, we extracted the contemporaneously collocated ABI, Landsat-8, and 375-m VIIRS active fire detections. To do this, we first remapped the Landsat-8, and 375-m VIIRS active fire detections into the ABI fixed grid projection. All the ABI fire pixels (not including low possibility detections due to large commission error, see section 4.2) were then removed if they were outside a ±2.5 min temporal window of either the Landsat-8 or S-NPP overpass times. For a remaining ABI fire pixel that collocated at least one Landsat-8 or 375-m VIIRS fire detection, it was flagged as a contemporaneous fire pixel. Otherwise, the ABI pixel was flagged as a no-contemporaneous fire pixel. The number of collocated Landsat-8 and 375-m VIIRS fire detections within the ABI fire pixel were also counted separately.

Second, the logistical regression models, which have been commonly used in the binary classification that aims to predict the probability of discrete outcomes (e.g., Yes/No, Positive/Negative, etc.) (Bishop, 2006), were established for calculating the ABI fire detection probability:

$$p(x_i) = \frac{1}{1+e^{-(\beta_0 \quad \beta x_i)}} \tag{2}$$

where $p(x_i)$ is the probability of considering the ith ABI pixel as a fire pixel, x_i is the count of contemporaneously collocated 30-m Landsat-8 (or 375-m VIIRS) active fire pixels, β_0 and β_1 are model parameters.

The β_0 and β_1 were solved using the gradient descent optimization method (Cauchy, 1847) with the ABI pixel flag (contemporaneous as “1” and no-contemporaneous as “0”) and the count of the extracted Landsat-8 or 375-m VIIRS fire detections. A training accuracy was calculated as the percentage of the correctly predicted samples by the best-fitted logistical regression models for all training data (x_i).

ABI might not be able to detect the fires observed by Landsat-8 or 375 m VIIRS within the ±2.5 min temporal window but it could detect them in a longer temporal window due to obscuration of clouds and change in fire phases (i.e., smoldering/flaming). Thus, we also investigated the ABI fire detection performance by relaxing the temporal window from ±2.5 min to ±8 hr (in the same day) to extract the collocated Landsat-8 and 375-m VIIRS active fire detections. A longer temporal window of ±8 hr was chosen to ensure that the matching window was longer enough to cover the period from 7 am - 9 pm local time during which the majority of fires occurred across southeastern CONUS (presented in Fig. 11).

3.2. Estimation of Error Rates of the GOES-16 ABI Active Fire Data

The omission and commission errors of the GOES-16 ABI active fire data was estimated using the error matrix approach that examines the overall accuracy of classification results of remote sensing data (Congalton, 1991). For the error matrix in this study, the 30-m Landsat-8 and 375-m VIIRS active fire data were taken as the “ground-truth” references and the collocated 2 km ABI fire data were the “classified” data. To determine if a 2-km ABI fire pixel was correctly detected, compatible 2-km “ground-truth” reference Landsat-8 and VIIRS fire masks were required. However, it was very challenging to define the “fire” in a 2-km pixel using 30-m Landsat-8 and 375-m VIIRS active fire data. By following the method proposed by Morisette et al. (2005b), we set up dynamic thresholds of the minimal number of Landsat-8 and VIIRS fire detections to derive a set of 2-km fire masks, where the minimal number varied from 1 to 500 for Landsat-8 and from 1 to 41 for VIIRS active fire detections. For example, a threshold of five would indicate that a 2km ABI pixel would need to include five or more Landsat fire detections to be classified as a fire pixel, otherwise as no fire if less than five detections. Then, an error matrix was obtained for each 2-km Landsat-8 and VIIRS fire mask and the associated omission and commission errors were estimated using eq. (3) and eq. (4), respectively.

$$E_o = \frac{M}{N} \times 100\% \tag{3}$$

where E_o is the omission error in percentage, M is the number of fire pixels in a 2-km Landsat-8 or VIIRS fire mask that has no contemporaneously collocated 2-km ABI fire pixel, and N is the total number of fire pixels in a 2-km Landsat-8 or VIIRS fire mask.

$$E_c = \frac{K}{N} \times 100\% \tag{4}$$

where E_c is the commission error in percentage, K is the number of the 2-km ABI fire pixels that have no contemporaneously collocated fire pixels in a 2-km Landsat-8 or VIIRS fire mask, and N is the same as in eq. (2).

Error rates of ABI fire detections for different categories were examined subsequently. Among the six categories of ABI fire detections, fire pixels flagged as processed, saturated, and cloud contaminated are theoretically considered as fire detections in the ABI fire detection algorithm while fire pixels labeled as high possibility, moderate possibility, and low possibility are considered as potential fire pixels due to failure in certain tests of the algorithm (Schmidt et al., 2012). Note that a cloud contaminated fire pixel is flagged when the pixel, which is obscured by cloud, has strong thermal signal that passes tests of the ABI fire detection algorithm (Schmidt et al., 2012). Thus, we first grouped the six categories into four groups: (1) fire detections (processed, saturated, and cloud contaminated), (2) high possibility, (3) moderate possibility, and (4) low possibility. Then, commission error was calculated for the four groups separately to show the false alarm error in each group detections. However, an omission error for each group detections is not able to reveal the performance of the ABI fire detection algorithm because fires missed by one group detections could be observed by another group detections. Instead of calculating omission error for each group separately, we first calculated omission error for group 1 that was taken as a base, and then for groups 1 and 2 together, and next for groups 1, 2, and 3 together, and finally all the four groups together. This helps to examine how omission error changes when different group fire detections are considered.

3.3. Comparison with Ground Records of Prescribed Fires

We compared satellite-based active fire observations with the ground-based prescribed-burning records in Georgia and Florida States. This comparison is challenging due to the uncertainties of the burning time, duration, and geolocation in the prescribed-burning records, and fire detection capabilities of satellites. For example, the burn could actually occur anytime between the planned start and end times and could even be canceled by the permit holder for personal reasons (Huang et al., 2018) and the geolocations were generally located about 0.5-1.0 km or even farther away from the actual burn location (Nowell et al., 2018). Moreover, a prescribed fire could be missed by a satellite due to obscuration of cloud and forest canopy and very low fire intensity. With all these in mind, we first selected significant burnings from 25 cloud free (or limited cloud cover) days during the study period using the NASA Worldview (https://worldview.earthdata.nasa.gov/) that is an online tool for quickly browsing most of the NASA products including VIIRS active fire data and true-color images. We then spatially matched the daily prescribed-burning records with the active fire detections from 375 m and 750 m VIIRS, contemporaneous ABI (within ±2.5 min of VIIRS overpasses), and daily ABI (all observations during an entire day). The ABI fire detections flagged as low possibility were excluded due to its very high commission error (see Section 4.2). (Note that we did not use Landsat-8 active fire data here mainly because the Landsat-8 data from each overpass cover less than one third of Georgia or Florida State and are available every 16 days). After all the daily prescribed-burning records were buffered by 2 km to reduce the uncertainty of the geolocations, a ground record was considered as being spatially matched with satellite fire detections if at least one satellite detection was found within its associated buffer. This process was performed for the active fire detection data from ABI, 375 m and 750 m VIIRS separately. The matched ground records were stratified by the planned size to burn (five groups: 1-50, 50-100, 100-200, 200-500, and > 500 acres) for both Georgia and Florida, and further by the planned start time (every hour) for Georgia and by burn purposes (agricultural, silvicultural, and land clearing) for Florida. Finally, the proportion of the matched records was calculated and compared for the groups and satellites.

3.4. Assessment of the GOES-16 ABI FRP Retrievals

To evaluate the capability of the GOES-16 ABI FRP estimation, we compared the ABI FRP retrieval with the 750-m VIIRS FRP retrieval in individual fire clusters and at a regional scale, separately. The 375-m VIIRS FRP was not used here because it was derived from the radiances of the collocated 750-m pixels at the VIIRS 4-μm M-band (see section 2.3) and has not been evaluated yet (Schroeder and Giglio, 2017).

The ABI FRP was first evaluated using 750-m VIIRS FRP in 211 fire clusters. A fire cluster was referred as to a group of spatially clustering active fire detections, which could consist of several small fires or parts of a big fire event. The fire clusters were manually extracted using a similar way to the approach used in Li et al. (2018), which was illustrated in Fig. 5. Specifically, we overlaid the fire detections that were collected contemporaneously by ABI and VIIRS within a ±2.5 min temporal window on the top of a 750-m VIIRS false-color composite (R: 2.25-μm band M11, G: 0.865-μm band M07, and B: 0.555-μm band M04). Then, the contemporaneous fire detections clustering around one or several fire pixels (red or orange color) on the VIIRS false-color image were manually enclosed using a polygon that was considered as a fire cluster (Fig. 5a). As a result, a total of 211 fire clusters were extracted (Fig. 5b). The contemporaneous FRP from ABI and 750 m VIIRS were separately summed up for each extracted fire cluster.

Finally, the cluster FRP estimates were statistically compared using the reduced major axis (RMA) regression method that minimizes error in both dependent (the ABI cluster FRP) and independent (the VIIRS cluster FRP) variables (Smith, 2009). The Pearson's correlation coefficient (r) was also calculated as an indicator of correlation between the two sensors' cluster FRP estimates.

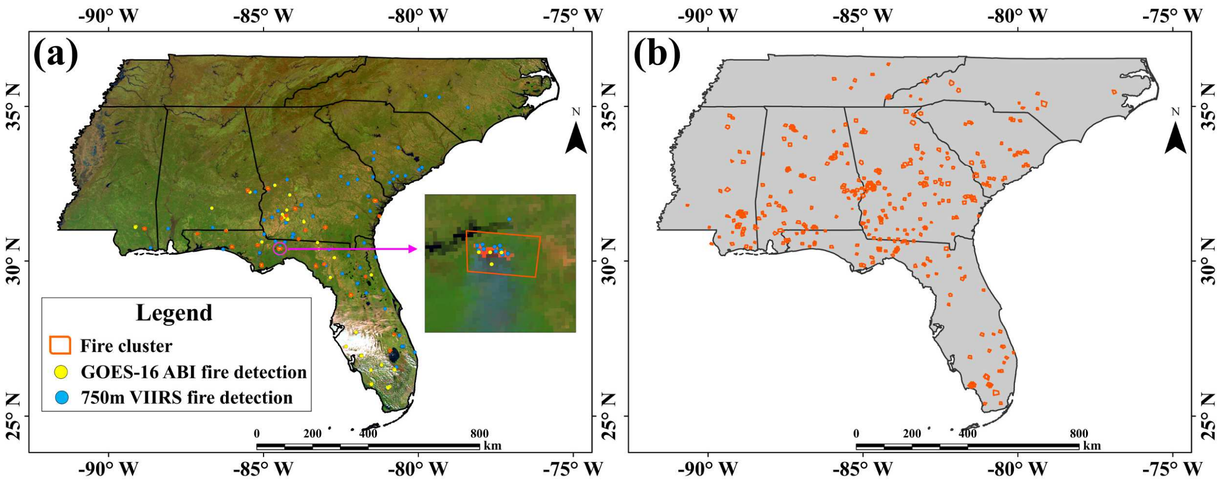

Fig. 5. Extraction of contemporaneous fire clusters. (a) shows an example of manually extracting fire clusters using the contemporaneous ABI and 750-m VIIRS fire detections collected at ~18:10 (UTC) on 03/02/2018. The square-shape image zooms in an extracted fire cluster highlighted using magenta circle in the map. (b) shows the distribution of the extracted 211 fire clusters across the southeastern CONUS.

We further evaluated ABI FRP using 750-m VIIRS FRP at a regional scale based on fires for the whole region of the southeastern CONUS. Specifically, to ensure that the two sensors observed fires contemporaneously, the ABI fire detections collected within ±2.5 min of the VIIRS observing time were clipped using the boundaries of the 750-m VIIRS daytime granules over the study region. The VIIRS granules were built using the 750-m VIIRS geolocation data.

The FRP retrievals of the contemporaneous fire detections were summed up separately for the two sensors to obtain regional FRP estimates. This process was repeated for each of the 25 days that were selected in Section 3.3. The regional FRP estimates were statistically compared using the RMA regression as the way in the cluster FRP comparison.

In addition to the direct comparisons of ABI and VIIRS FRP in individual fires and at a regional scale, we also conducted a FRP frequency-magnitude analysis using FRP retrievals from contemporaneous ABI and 750-m VIIRS active fire detections following Roberts and Wooster (2008) and Freeborn et al. (2009). Specifically, contemporaneous ABI and 750-m VIIRS active fire detections were extracted in the process of evaluating the ABI FRP at a regional scale (see the previous paragraph). All the extracted contemporaneous ABI and 750-m VIIRS fire detections were then grouped into equal-width FRP bins (in log scale) by their FRP retrievals and the detection frequency was calculated for each group. The frequency-magnitude analysis helps to examine the distributions of the contemporaneous FRP retrievals and explore the low-limit fire detection capability of a sensor (Roberts and Wooster, 2008).

4 Results

4.1. Overall Fire Detection Performance of GOES-16 ABI

Table 2 lists the optimized parameters of four ABI detection probability models that were fitted using the contemporaneous fire detections of ABI against Landsat-8 and 375 m VIIRS. The contemporaneous Landsat-8 fire detections, which were extracted during the spatiotemporal-matching process (see Section 3.1), were located in a total of 1519 ABI pixels (82% and 0.9% of them with < 10 and ≥ 100 Landsat-8 detections, respectively). However, only 41 (or 2.7%) of these ABI pixels were detected as fire pixels by the ABI active fire algorithm within ±2.5min of Landsat-8 acquisition time and each of these ABI fire pixels contained 2- 489 Landsat-8 fire detections (with a median of 83) (Fig. 6a). Similarly, the extracted contemporaneous 375-m VIIRS fire detections were distributed in a total of 8195 ABI pixels of which 1030 (or 12.5%) were detected as ABI fire pixels within ±2.5 min of the VIIRS observing time (Fig. 7a, b). When the temporal window (difference in observing time between ABI and Landsat-8 or VIIRS) was relaxed from ±2.5 min to ±8 hr, the number of the matched contemporaneous ABI fire pixels increases from 2.7% to 11.2% (Fig. 6c) and from 12.5% to 39.8% (Fig. 7c) by referencing 30-m Landsat-8 and 375-m VIIRS fire detections, respectively. The accuracy of the fitted models based on Landsat-8 data is overall higher than that based on 375-m VIIRS data.

Table 2. The detection probability models of the ABI sensor established based on 30-m Landsat-8 and 375-m VIIRS fire detections.

Satellite	Temporal window	Model parameters		Training accuracy
		β_0	β_1	
Landsat-8	±2.5 min	-5.092281	0.032602	99.3%
	±8 hr	-3.079540	0.031031	95.3%
VIIRS	±2.5 min	-3.490842	0.474086	92.7%
	±8 hr	-2.244143	0.556000	79.1%

The fire detection probability of the ABI sensor increases as the count of contemporaneous referencing fire detections grows. Fig. 6e and 7e illustrate the variations of the ABI fire detection probability characterized by the four fitted models. All these models show a common pattern that the ABI fire detection probability generally increases as the count of contemporaneous 30-m Landsat-8 and 375-m VIIRS fire detections within an ABI pixel increase. Within a ±2.5 min temporal window, the ABI detection probability increases from ~5-95% and from ~0.3-95% as the count of contemporaneous Landsat-8 and 375-m VIIRS fire detections grows from 1-114 and from 1-11, respectively. When an ABI pixel contains less than 50 Landsat-8 or five 375-m fire detections, the ABI detection probability is less than 14% and 37%, respectively (Fig. 6e, and Fig. 7e). This is also reflected in the histogram of the not-matched Landsat-8 fire detections that are mostly less than 50 (Fig. 6b) and histogram of the not-matched 375-m VIIRS fire detections that are less than five (Fig. 7b).

The ABI sensor observes many more fires that are detected by Landsat-8 and VIIRS as the temporal window of ABI observations relaxes from ±2.5 min to ±8 hr. Specifically, the number of Landsat-8 fire detections matched by the ABI fire detections increases by ~19% from 4374 (32.6%) to 6886 (51.4%) (Fig. 6a, c). For ABI fire pixels containing less than 50 Landsat-8 fire detections, the number of the Landsat-8 fire detections matched by these ABI fire pixels increases by a factor of 12 (Fig. 6a, c). Similarly, the number of 375-m VIIRS fire detections increases by ~29% from 4769 (28.2%) to 9776 (57.9%) (Fig. 7a, c). For ABI fire pixels containing less than five 375-m VIIRS fire detections, the number of 375-m VIIRS fire detections matched by these ABI fire pixels increases by a factor of four (Fig. 7a, c).

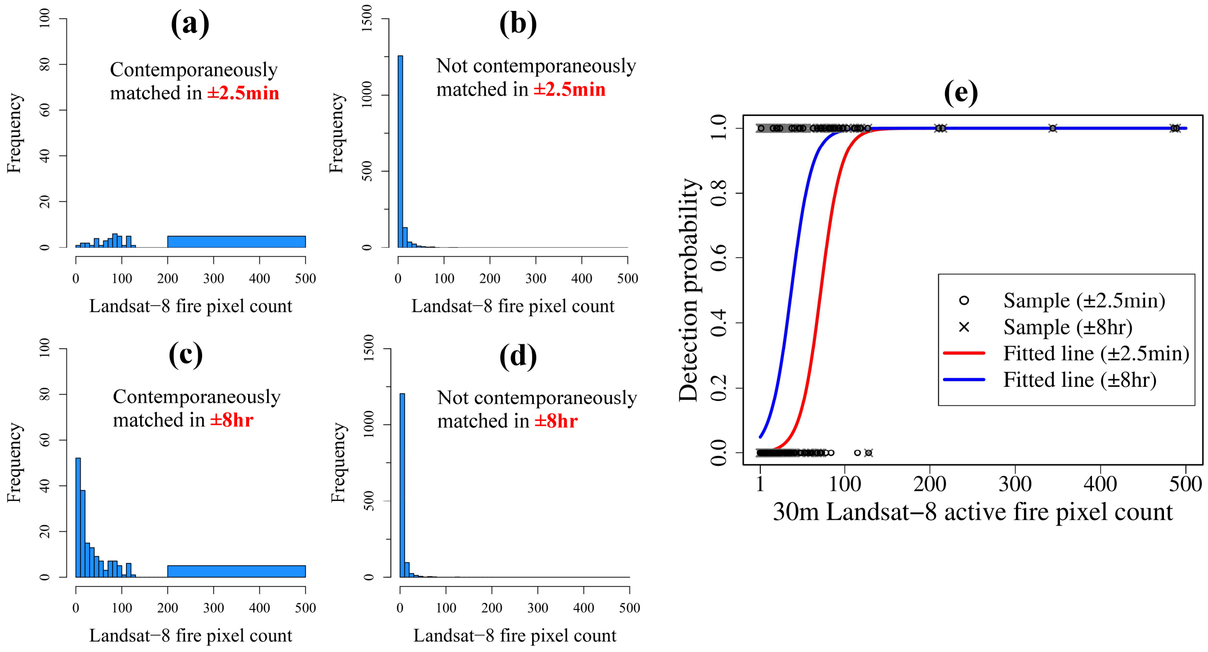

Fig. 6. The ABI fire detection probability modeled using fire pixels detected contemporaneously by ABI and Landsat-8. (a-b) show histograms of the count of the 30-m Landsat-8 fire pixels within a 2-km ABI pixel that was detected as either an ABI fire pixel or a non-fire pixel within ±2.5 min of the Landsat-8 observing time. (c-d) display the same information as (a-b) but for an 8 hr observing time difference. (e) shows the ABI fire detection probability within a temporal window of the ±2.5 min (red line) and ±8 hr (blue line), respectively.

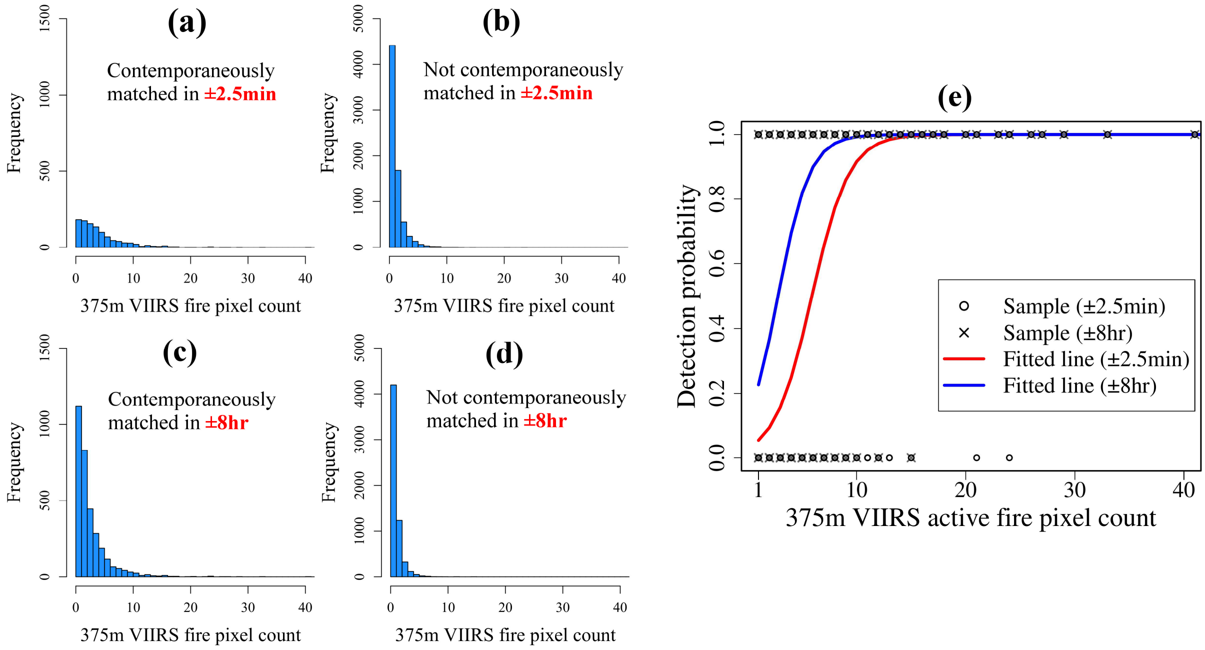

Fig. 7. The ABI fire detection probability modeled using fire pixels detected contemporaneously by 2 km ABI and 375 m VIIRS. (a-e) show the same information as (Fig. 6a-e) but for the 375-m VIIRS fire pixels.

4.2. Omission and Commission Errors

Fig. 8 shows the variation of omission error probability of the ABI active fire data with a dynamic threshold of the 30-m Landsat-8 (left column) and 375-m VIIRS (right column) fire detection count in a 2-km resolution. The ABI omission error generally decreases as the dynamic threshold of the 30-m Landsat-8 or 375-m VIIRS fire detection count increases. For instance, within a ±2.5 min temporal window of the Landsat-8 acquisition time, the omission error of the ABI group 1 (processed, saturated, and cloud contaminated) fire detections decreases from 97% to 14% as the dynamic threshold increases from one to 150 pixels, and further decreases sharply to zero as the threshold is larger than 150 (Fig. 8a). Similarly, as the dynamic threshold of the

375-m VIIRS fire detection count increases from one to 15, the omission error of the ABI group 1 fire detections decreases from 87% to 16% correspondingly and it becomes zero when the threshold of the 375-m VIIRS fire detection count is larger than 25 (Fig. 8b). With considering ABI group 2 (high possibility), the ABI omission error for groups 1 and 2 overall reduces with a decrease of up to 7% for 30-m Landsat-8 and 8% for 375-m VIIRS (Fig. 8c, d). If including the ABI group 3 (moderate possibility), the ABI omission error for groups 1-3 does not change for the 30-m Landsat-8 (Fig. 8e) and changes very little for 375-m VIIRS (Fig. 8f), because the ABI detections with moderate possibility are very limited. By taking the ABI group 4 (low possibility) detections into account (or all ABI fire detections), the ABI omission error for groups 1-4 further reduces by up to 14% for 30-m Landsat-8 and 15% for 375-m VIIRS (Fig. 8g, h).

Further, for both the Landsat-8 and 375-m VIIRS fire detections, the associated ABI omission error is significantly reduced as the temporal window is relaxed to from ±2.5 min to ±8 hr (Fig. 8). For instance, the omission error for the ABI group 1 detections decreases by up to 33% and 34%, respectively, by referencing the Landsat-8 and 375-m VIIRS (Fig. 8a, b). If the ABI group 2, 3, and 4 detections are also considered in order, the reduction percent of the omission error decreases gradually.

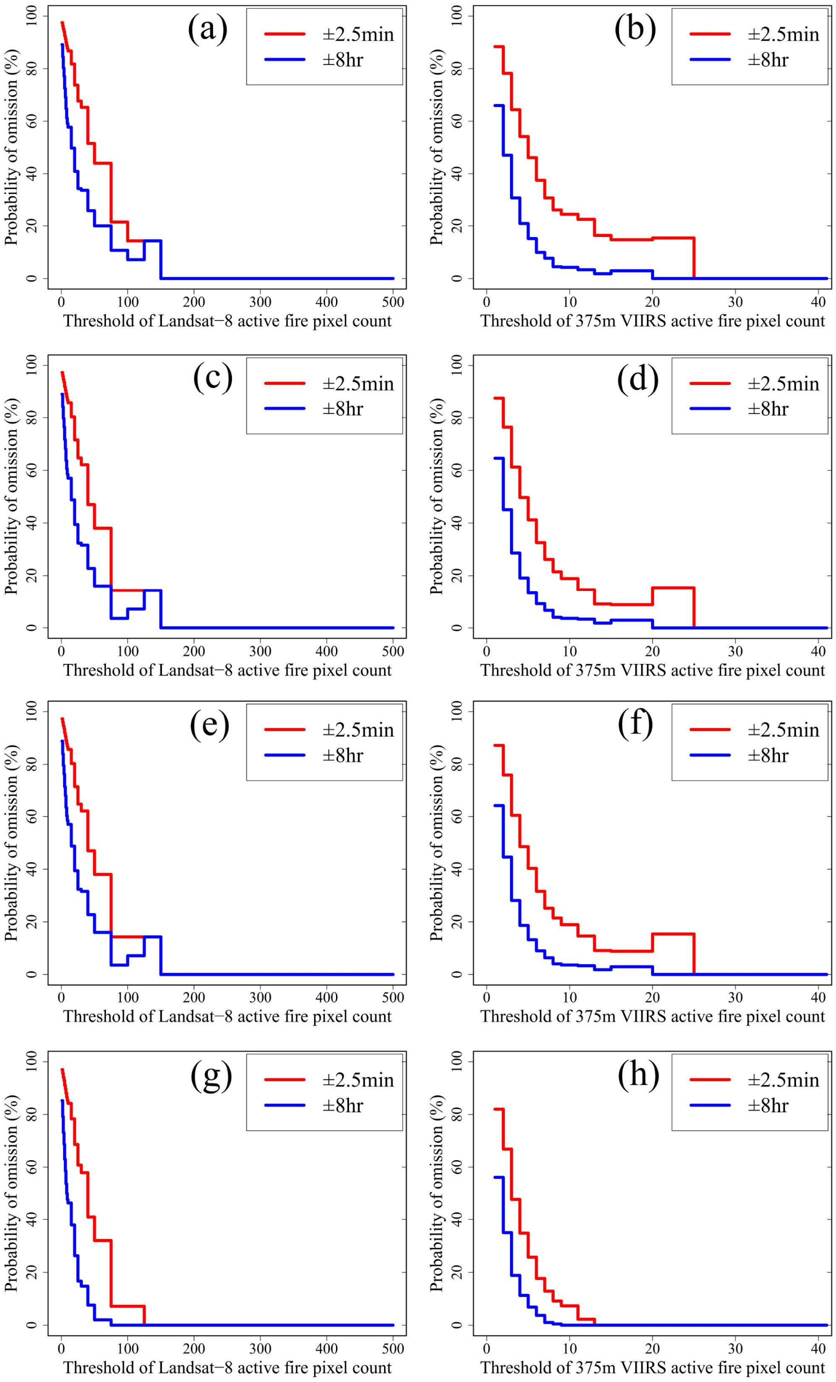

Fig. 8. Variations of the omission error probability of the ABI fire detections. The probability of omission errors estimated by comparing with the contemporaneous 30-m Landsat-8 fire detections (a, c, e, and g) and 375-m VIIRS fire detections (b, d, f, and h). The omission error

probability varying with ABI fire detection categories: group 1 (a-b), groups 1-2 (c-d), groups 1-3 (e-f), and groups 1-4 (g-h).

The ABI commission error (or false alarm) based on the Landsat-8 and 375-m VIIRS active fire data shows a large discrepancy during the selected 25 days. Within a ±2.5 min temporal window of Landsat-8 acquisition time, the ABI commission error is 1% for group 1, 1% for group 2, 3% for group 4. The commission error for group 3 is not calculated because of no contemporaneous ABI fire detections. However, within ±2.5 min of VIIRS overpass time, the ABI commission error is 14%, 15%, 21%, and 71% for the group 1, 2, 3, and 4 detections, respectively. Fig. 9 as an example illustrates the distributions of ABI fire detections spatially matched and not matched (false alarms) with the 375-m VIIRS fire detection within a ±2.5 min temporal window. The false alarms for the ABI group 1 fire detections are mainly distributed along the boundaries between Georgia, Alabama, and Florida States and in southern Florida and southwestern South Carolina (Fig. 9b), which is similar to the spatial distribution of the matched ABI detections (Fig. 9a). Among these identified false alarms, 23% of them occur in the locations where both ABI and VIIRS detected fires during previous days and 39% of them occur in the adjacent pixels of these locations (pink dots in Fig. 9b). For the ABI groups 2 and 3 fire detections, the false alarms mainly occur in North Carolina and Tennessee (Fig. 9c, d). The ABI false alarm for group 4 fire detections is 4 - 14 times higher than that in the other three groups, where 85% of false alarms are located in North Carolina (40%), Georgia (21%), South Carolina (16%), and Tennessee (8%) (Fig. 9e).

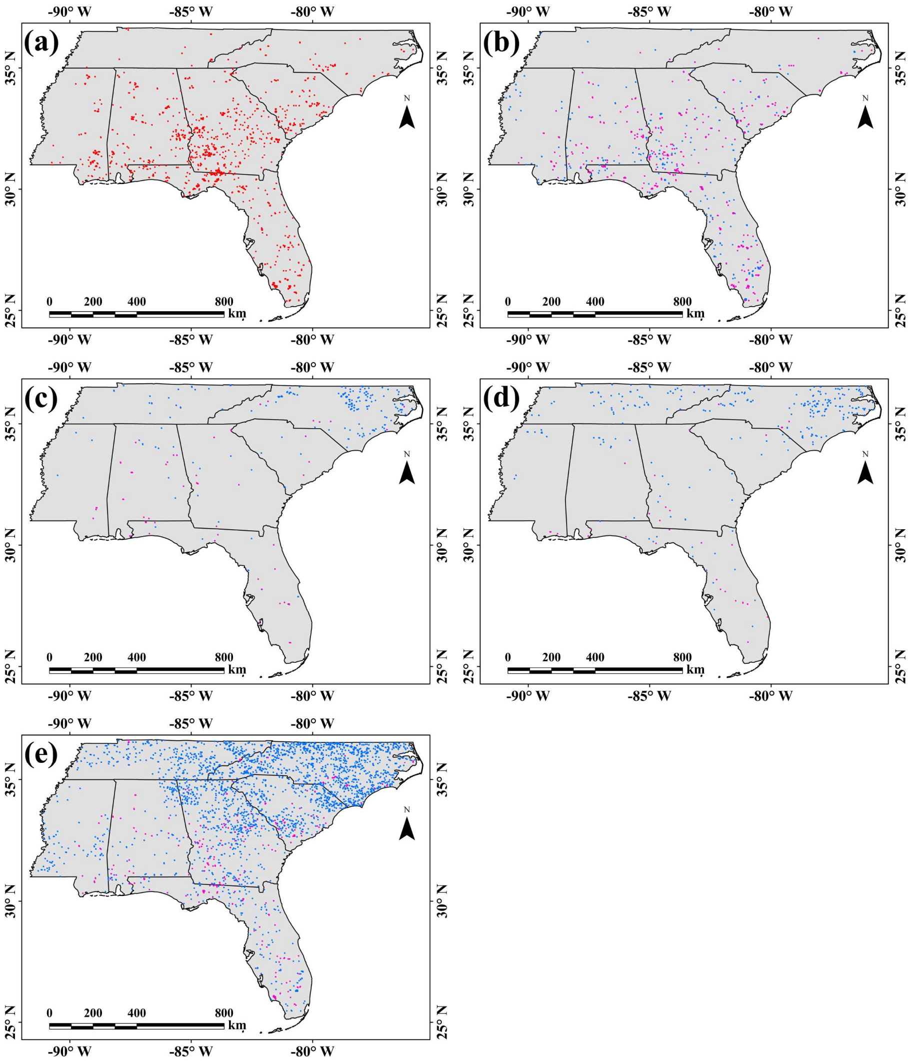

Fig. 9. ABI fire detections spatially matched and not matched (false alarms) with the 375-m VIIRS fire detection within ±2.5 min of VIIRS daytime overpasses in the selected 25 days across the southeastern CONUS. (a) Matched ABI fire detections. (b-e) Not-matched ABI fire detections for group 1 (b), group 2 (c), group 3 (d), and group 4 (e). In (b-e), pink dots show ABI false alarms that occurred in the same locations where both ABI and VIIRS detected fires in previous days or occurred in the adjacent pixels of these locations, and blue dots indicate ABI false alarms that were far away from these locations.

4.3. Satellite active fire detections spatially matched with ground burning records

ABI active fire detections are further assessed by comparing with ground burning records in Georgia and Florida States. Fig. 10 shows the daily count of GOES-16 ABI, 375-m and 750-m VIIRS fire detections, and prescribed burning permits during the study period across Georgia (all acreage burning permits including the not-geolocated permits) and Florida (all burning permits for at least one-acre fires). In the both States, the daily counts of satellite active fire detections mostly vary similarly with the number of prescribed burning permits. Note that in Georgia the count of ABI fire detections has a very high peak on April 16 when both the two VIIRS fire products and prescribed-burning permits show very small numbers (Fig. 10a). This abnormal peak of the ABI fire detections on April 16 is due to a large number of false alarms. However, April 16 is not among the selected days in analyses conducted in this study and thus the abnormal ABI false alarms do not affect results presented in Section 4.

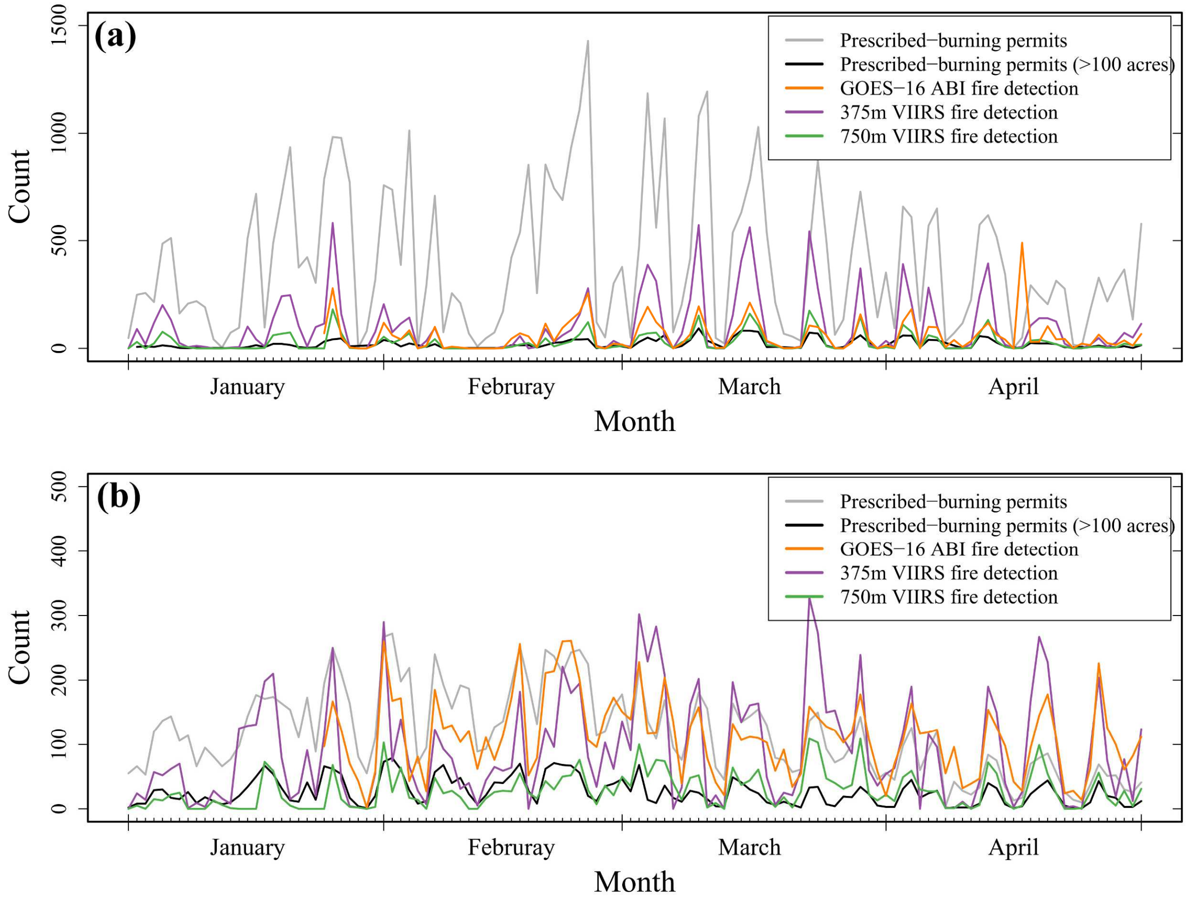

Fig. 10. Daily count of the prescribed-burning permits and satellite active fire detections in Georgia (a) and Florida (b) States from January-April 2018.

The proportion of prescribed-burning records spatially matched with ABI and VIIRS active fire data varies with the hour of the planned start burning time. In Georgia, the 750-m VIIRS and 375-m VIIRS fire detections match 12% and 25% of all the 3133 ground burning records, respectively. Within a ±2.5min temporal window of VIIRS overpass, the ABI fire detections match only 2% of ground burning records. If all daily ABI fire observations (not including “low possibility”) are considered, the percent of ground burning records matched by the ABI fire detections increases to 29%. The ABI diurnal fire detection profile starts at around 8:00, ends at 21:00, and peaks between 13:00 and 14:00 local time (Fig. 11b), which is consistent with the planned start and end burning times of ground burnings that range from 7:00 - 16:00 and from 15:00 - 21:00 local time and peak at 10:00 and 19:00, respectively (Fig. 11a). During a day, all three-type satellite fire data match larger proportion of prescribed-burning records in the morning than afternoon (Fig. 11a, c). On an average hourly basis, the ABI detections match 8% and 17% less ground burning records than the 750-m and 375-m VIIRS detections, respectively, within ±2.5min of VIIRS overpass but the ABI matched proportion increases by 23% when all daily ABI fire observations are considered (Fig. 11c). Although all three-type satellite fire data match less than 40% of burns in all hours, the ABI detections match more ground records than both the 750-m and 375-m VIIRS active fire data, especially in noon and afternoon hours after 11:00 (Fig. 11c).

Furthermore, the proportion of prescribed-burning records spatially matched with ABI and VIIRS active fire data increases with the size of the area planned to burn in both Georgia and Florida. In Georgia, the prescribed-burning records planned to burn an area ranging from 1-2500 acres (~0.004 - 10.1 km^2) and 95% of burns are smaller than 100 acres (~0.404 km^2) (Table 1 and Fig. 11d, e). Almost all burns larger than 100 acres are geolocated, which is consistent with the geolocation requirement of the GFC's acreage burning permits. As the size of the area planned to burn increases, all three-type satellite fire data matched larger proportion of prescribed-burning records (Fig. 11f). Among the three-type satellite fire detection data, the ABI fire data on average match 21% and 37% less than the 750-m and 375-m VIIRS active fire data, respectively, within ±2.5min of VIIRS overpass but match 22% and 6% more when all daily ABI fire observations are considered in five different-size groups (Fig. 11f).

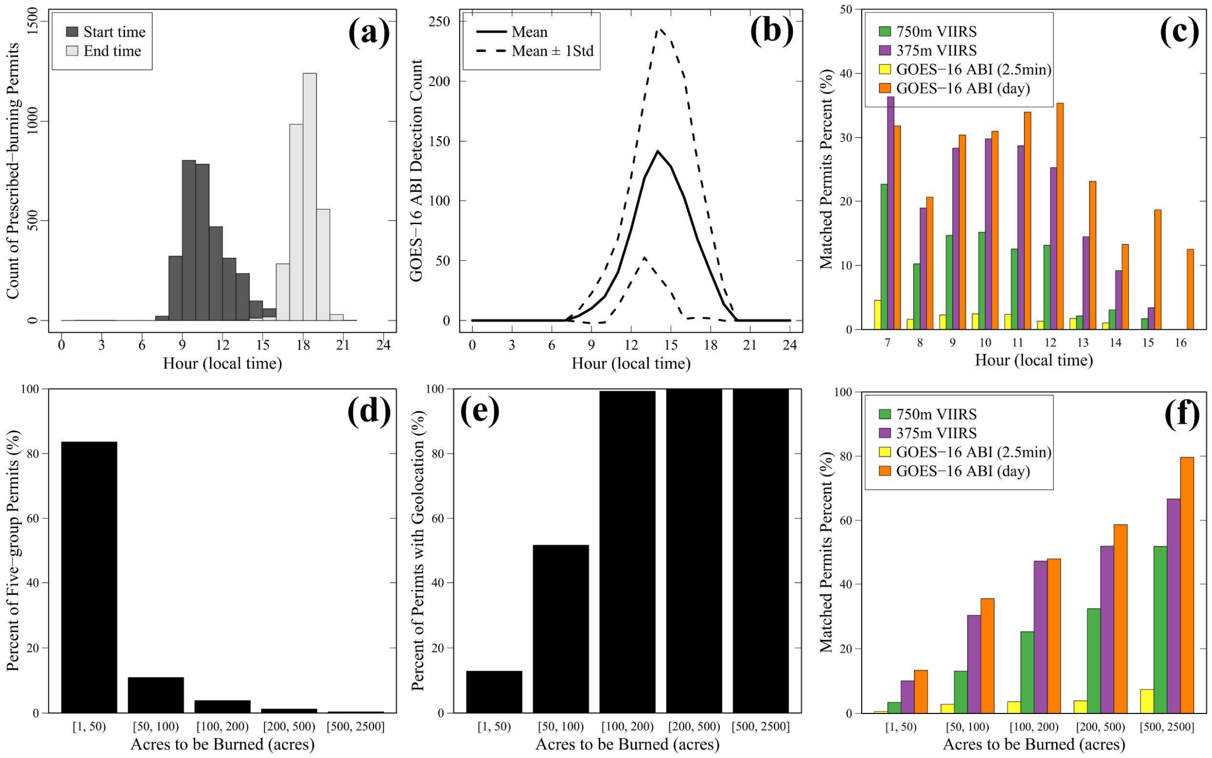

Fig. 11. The satellite active fire detections spatially matched with the prescribed-burning permits in Georgia State during the selected 25 days. (a) The number of geolocated prescribed-burning permits varying with the planned start and end burning times. (b) The diurnal profile of ABI fire detections characterized by hourly mean detection count. (c) The percent of prescribed-burning permits spatially matched with satellite active fire detections, varying with the planed begin burning times. (d), (e), and (f) are the percent of burning permits in five groups stratified by size of area planned to burn, with geolocations in each group, and spatially matched with satellite active fire detections in each group, respectively. Note the terms “2.5min” and “day” in legend represent GOES-16 ABI fire detections observed within ±2.5min of VIIRS overpass time and during all day, respectively.

In Florida, the percent of ground burning records matched by all three-type satellite fire data also generally increases with the size of area planned to burn (Fig. 12). For all the 2903 burning permits recorded in the selected 25 days, the percent of records matched by the 750-m and 375-m VIIRS active fire data is 14% and 25%, respectively (Fig. 12a). In contrast, the percent of ground burning records matched by the ABI fire detections within ±2.5min of VIIRS overpass is only 3% but increases to 56% (or 42% and 31% more than the 750-m and 375-m VIIRS active fire data) after considering all ABI fire observations during a day (not including "low possibility") (Fig. 12a). Moreover, for silvicultural burning records, the percent of records matched by ABI fire data within ±2.5min of VIIRS overpass is on average 29% and 48% less than the 750-m and 375-m VIIRS active fire data, respectively (Fig. 12b). However, the percent of ground burning records matched the ABI fire observations during a day is 57%, which is comparable to that matched by 375-m VIIRS (56%) although the 375-m VIIRS fire data match slightly more fires smaller than 200 acres (Fig. 12b).

As for agricultural burning records, fires smaller than 200 acres are dominated by sugarcane related burnings (72%) and larger fires are mainly related to management of pasture and rangeland. The percent of ground burning records matched by the 750-m and 375-m VIIRS active fire data is 19% and 28%, respectively. In contrast, the percent of ground burning records matched by the ABI detections within ±2.5min of VIIRS overpass is on average 9% but increases to 75% after considering all ABI fire observations during a day (not including "low possibility") (Fig. 12c). The percent of matched ground burning records after considering all daily ABI fire detections increases for fires smaller than 200 acres but decreases gradually for larger fires (Fig. 12c). This pattern contrasts with the consistently increasing trends of the percent of ground burning records matched by ABI with fire size in silvicultural burnings (Fig. 12b) and burnings for all three purposes (Fig. 12a).

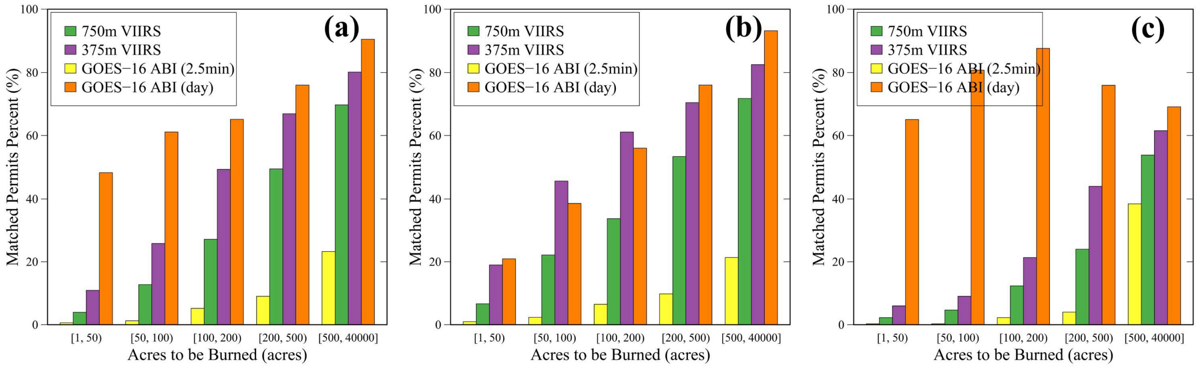

Fig. 12. The prescribed-burning permits spatially matched by GOES-16 ABI and VIIRS 375m and 750m active fire detections in Florida State during the selected 25 days. The percent of the spatially matched burning permits varying with five-stratified groups of area size planned to burn: (a) for all purposes (silvicultural, agricultural, and land clearing), (b) for silvicultural purpose, (c) for agricultural purpose. Note the terms “2.5min” and “day” in legend are the same as in Fig. 11.

4.4. FRP Frequency-magnitude Relations

Fig. 13 shows the FRP frequency density distributions of the fire detections contemporaneously observed by 2 km ABI and 750 m VIIRS. The ABI and 750-m VIIRS FRP (per pixel) varies from ~20 – 1211 MW and from ~2.3 – 543 MW and peaks at ~34.5 MW and ~7.1 MW, respectively. The peak frequency density suggests the low-limit FRP that a sensor is able to detect confidently. It is evident that the 750-m VIIRS FRP frequency is much higher than the ABI FRP frequency in the FRP bins between 2 and 30 MW, indicating VIIRS is able to observe many small and cool fires with a FRP less than the ABI low-limit.

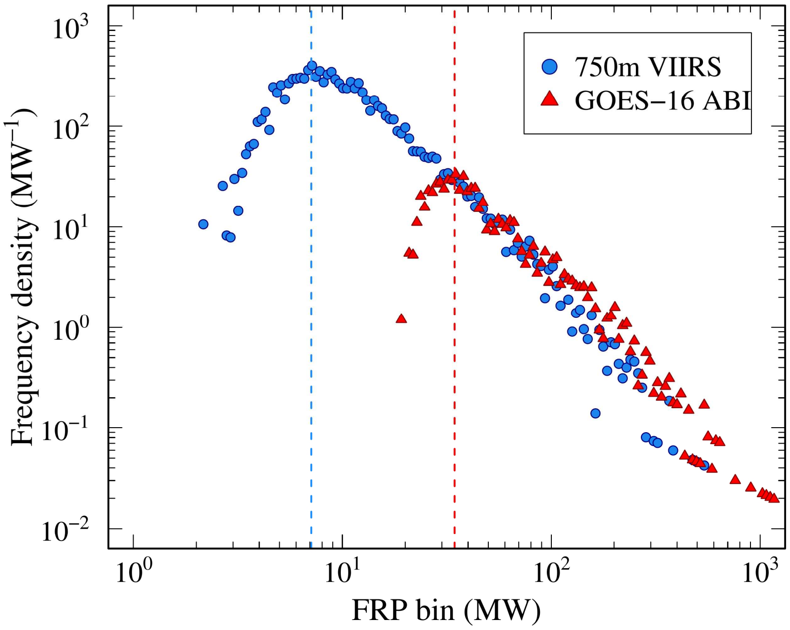

Fig. 13. Frequency density of the contemporaneous ABI and 750-m VIIRS pixel-level FRP. The red and blue dashed vertical lines respectively show the occurrences of the maximum frequency density at FRP bins of the ABI (34.5 MW) and 750 m VIIRS (7.1 MW).

4.5. Comparison of Fire Cluster FRP

Fig. 14 illustrates the comparison of contemporaneous FRP estimates in individual fire clusters. In the selected 211 fire clusters, the ABI and 750-m VIIRS FRP estimates are strongly correlated (*Pearson* $r = 0.88$). The best-fitted model suggests that the ABI FRP is overall ~30-50% larger than the 750-m VIIRS FRP with an insignificant bias ($p_{constant} = 0.518$ and its 95% confidence interval includes zero), but the 750-m VIIRS cluster FRP is larger than the ABI FRP in more than 50 fire clusters. Moreover, the fire-cluster FRP relationship between the two sensors shows no dependence on ABI VZA, which is evident in the evenly distributed fire clusters with different ABI VZA.

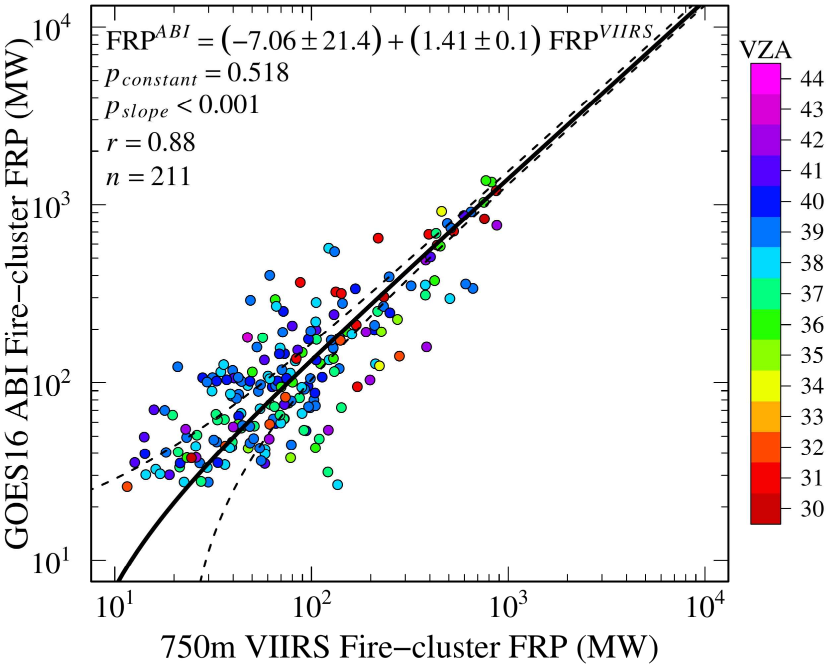

Fig. 14. Comparison of the contemporaneous ABI and 750-m VIIRS FRP estimates in the selected 211 fire clusters. The fire clusters were sensed by the two sensors within a ±2.5 min observing time difference and are colored by ABI view zenith angle ranging from 30° to 44°. The black solid line is the best-fitted line and the black dashed lines show the lower and upper bound of the fitted line in a 95% confidence interval (CI). For the best-fitted model, the values after "±" are the 95% CIs of the constant and slope coefficients whose p-values are the $p_{constant}$ and p_{slope}, respectively.

4.6. Regional-scale FRP Comparison

The contemporaneous FRP estimates from ABI and 750-m VIIRS are generally comparable at the regional scale across the southeastern CONUS (Fig. 15). The daily regional ABI FRP that was cumulated within ±2.5 min of the VIIRS overpass time is merely 1% different from the regional 750-m VIIRS FRP. The bias (or the constant coefficient of the best-fitted model) is insignificant ($p_{constant} = 0.416$) and its 95% confidence interval includes zero. Moreover, the regional FRP estimates from the two sensors are strongly correlated (*Pearson* $r = 0.91$).

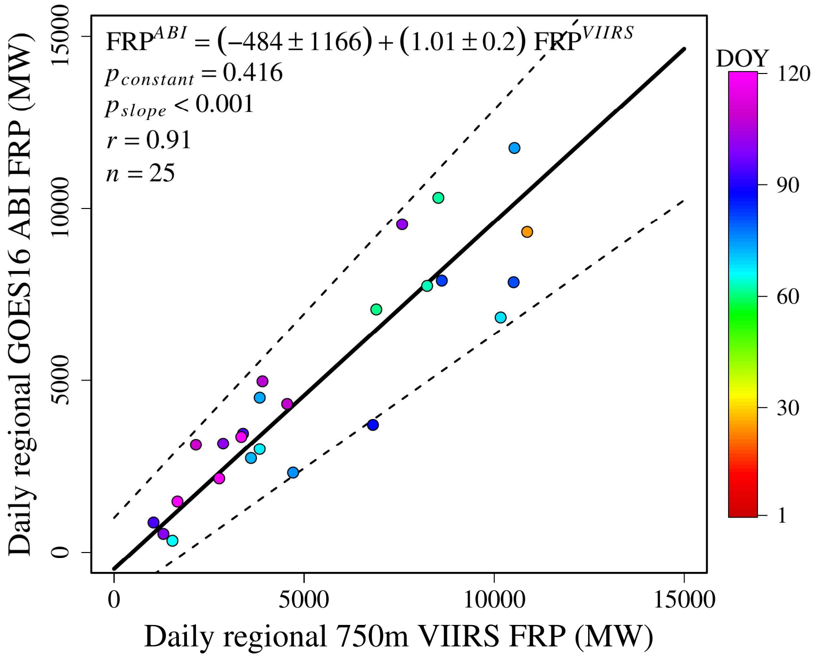

Fig. 15. Comparison of the contemporaneous ABI and 750-m VIIRS FRP estimates in the southeastern CONUS region during the selected 25 significant burning days. Each sample (filled circle) represents the daily cumulative FRP estimates of the fire detections contemporaneously observed by ABI and VIIRS within ±2.5 min and is colored with observing day of year (DOY). The black solid line is the best-fitted line and the black dashed lines show the lower and upper bound of the fitted line in a 95% confidence interval (CI). For the best-fitted model, the values

after "±" are the 95% CIs of the constant and slope coefficients whose p-values are the $p_{constant}$ and p_{slope}, respectively.

5 Discussion

5.1. The GOES-16 ABI Fire Detection Performance

The ABI fire detection performance is highly related to fire size. This is demonstrated by the fact that the ABI fire detection probability increases and the ABI omission error decreases with the number of Landsat-8 and 375-m VIIRS detections within an ABI pixel (Fig. 6e and 7e). This performance is similar to that of MODIS and the previous GOES (Morisette et al., 2005a, 2005b; Csiszar et al., 2006; Schroeder et al., 2008). Compared with other orbiting geostationary satellites, the ABI omission error based on the 375-m VIIRS fire detections is ~82% if one VIIRS detection is taken as the threshold to generate the 2-km VIIRS fire mask (Fig. 8h), which is higher than the MSG SEVIRI pixel product (65-77%) over Africa (Roberts et al., 2015) and the Himawari AHI (66%) over Asia and Australia (Xu et al., 2017) estimated using the 1-km MODIS fire detections. However, interpretation of fire detection performance among ABI, SEVIRI, and AHI should be very careful because omission errors of fire data from these sensors are estimated based on different higher-resolution fire detections over different regions. The 375-m VIIRS I-band has much higher spatial resolution and is less affected by the bow-tie effect compared with the 1-km MODIS, which enables the VIIRS I-band to observe more small/cool fires than MODIS (Schroeder et al., 2014). For instance, the 375-m VIIRS detects more than five times of MODIS fire detections in agricultural burnings in China (Zhang et al., 2017a) and India (Vadrevu and Lasko, 2018). Thus, the omission errors of the SEVIRI and AHI fire data would most likely increase if fire detections from 375-m VIIRS instead of MODIS had been used to estimate omission error, which can also be inferred from the fact that the ABI omission error increases when the evaluation fire data are switched from the 375-m VIIRS to the 30-m Landsat fire detections (Fig. 8). The commission errors (14-21%) of the ABI fire detections flagged as processed, saturated, cloud contaminated, high possibility , and moderate possibility are slightly higher than SEVIRI (9-13%) (Roberts et al., 2015) and AHI (8%) (Xu et al., 2017) but the low possibility ABI detections have much higher commission errors (71%). This confirms that most of the low possibility ABI detections are likely false alarms (Schmidt et al., 2012) and the usage of these detections in applications should be careful, although inclusion of the low possibility detections slightly reduces the ABI omission error (Fig. 8g, h). The commission error of the ABI active fire data could be partly related to thermal conditions changed by biomass burnings in preceding days. More than half of false alarms in the ABI group 1 fire detections are adjacent to or even located in the areas where both ABI and VIIRS had fire detections during preceding days (Fig. 9b), which is also found in small parts of groups 2-4 (Fig. 9c-e). This is possibly due to the thermal contrast between the areas burned in preceding days and vegetated background, which was also found in validation of the active fire data of a previous GOES satellite in Brazilian Amazonia (Schroeder et al., 2008). However, for groups 2-4 ABI fire detections, majority of the false alarms are far from precedent burn areas and are mainly located in the northeastern states, especially North Carolina (Fig. 9c-e), where the 375 m VIIRS detected significantly fewer fires in the selected 25 days (not shown here). The causes are not clear and need to be investigated and corrected in the future versions.

Moreover, the ABI fire detection also performs better in matching ground-based burning records with the larger size of the planned area to burn (Fig. 11 and 12). As with the 375-m and

750-m VIIRS, the percent of ground burning records matched by ABI fire detections increases with the size of area planned to burn in both Georgia and Florida States (Fig. 11 and 12), which is similar to the increasing detection rate of ground burnings with fire size by GOES-13 and MODIS in Georgia (Hu et al., 2016). However, the ABI's detection percent of ground burnings (with a size < 500 acres or 2.02 km^2) is about two times of that by GOES-13 (Hu et al., 2016), which suggests a big improvement of GOES-R ABI over the legacy GOES satellites in fire detection. For agricultural burnings in Florida State, it is interesting that the percent of ground burning records with a size of 50-200 acres matched by ABI are higher than those records with a size larger than 200 acres when all the daily ABI detections are considered (Fig. 12c). This is likely related to the fuel difference between sugarcane-related fires and fires for management of pastures and rangelands. In Florida State, 72% of selected ground burnings with a size smaller than 200 acres are sugarcane-related fires that are generally set to clear sugarcane residuals before harvest and burn very intensely due to dense fuel loads. In pastures and rangelands, fires could burn a larger area (i.e., > 200 acres) than sugarcane-related fires but most are low-intensity fires because fuels are mainly short grasses with much lower fuel loads.

Although ABI could detect a large portion of large fires, the ABI fire data miss a large number of very small fires. In Georgia State, for example, ABI is able to detect only 29% of the fires planned to burn with a size larger than 100 acres (~0.404 km^2) that only account for less than 40% of total area planned to burn during the study period, and even 375 m VIIRS can detect only 25% of these fires (Fig. 11). Most likely ABI and VIIRS have a lower detection rate in detecting those burns smaller than 100 acres that contribute to more than 60% of total area planned to burn. This possibly explains the very large discrepancy between the satellite-based and ground-based burned area data in the southeastern CONUS (Huang et al., 2018; Nowell et al., 2018). For example, Nowell et al. (2018) suggests that the burned area in the Global Fire Emission Database (GFED) is smaller than the ground-reported burned area by a factor of three in Florida State, even though the study includes the MODIS active fire detection derived burned area by “small fires” in GFED (Randerson et al., 2012). Thus, it remains challenging to detect very small and cool fires using both active fire and burned area products from current satellites. The ABI’s missing very small fires could be mostly attributed to the fact that these small fires are beyond the ABI sensor’s detection capability. For instance, 82% of the ABI fire pixels contain less than 10 30-m Landsat-8 fire detections, which approximates a fire size of up to 0.009 km^2. The temperature for such small prescribed fires in the southeastern CONUS is typically less than 600 K (Kennard et al., 2005), while an average temperature higher than 700 K is needed for the ABI fire detection algorithm to detect the fire under cloud-free condition (Schmidt et al., 2012). This explains that the ABI generally misses fire detections for pixels containing less than 10 30-m Landsat-8 or five 375-m VIIRS fire detections (Fig. 6 and 7). This result is also supported by the fire detections from the Himawari-8 AHI (a sensor identical to ABI) that misses ~66% of low-intensity agricultural burnings across Asia (Xu et al., 2017).

The ABI fire detection performance is largely enhanced by its very high-temporal resolution. As the temporal window is relaxed from ±2.5 min to ±8 hr in the spatiotemporal-matching process with Landsat-8 and 375-m VIIRS fire detections, the ABI fire detection probability increases by up to 60% or more and its omission error decreases by up to 33% correspondingly (Fig. 6 and 7). This is consistent with the result that the omission error reduces when considering the temporal information in validation of active fire data of a previous GOES in Brazilian Amazonia (Schroeder et al., 2008). The enhanced ABI fire detections performance is likely associated with two factors. First, fire intensity (or temperature) is highly dynamic as fire activity is tightly related to fire weather (e.g., wind speed and relative humidity) (Pyne et al., 1996; Rothermel, 1972). Therefore, the 5min-resolution ABI could observe a fire when it is intense enough during a longer temporal window. Second, tree canopy attenuates radiative energy released from fires, reducing the chance of satellite fire detection (Mathews et al., 2016; Roberts et al., 2018), which particularly is the case for forest understory prescribed burnings across the southeast CONUS (Ryan et al., 2013). However, ABI could observe a fire as it spreads from dense canopy covered area to open spaces. Moreover, the enhancement of ABI fire detection performance is also revealed in comparing with ground prescribed-burning records, which indicates ABI detects more prescribed fires than VIIRS does when all the daily ABI fire detections are considered (Fig. 11 and 12) because many prescribed fires occurred during hours beyond the VIIRS overpass time (Fig. 11c).

Additionally, as with VIIRS and other satellite sensors, the ABI fire detection performance could be significantly impaired by cloud obscuration. For example, both ABI and VIIRS fire detections were very limited during the days, such as January 8-11 and February 7-28, although the count of prescribed-burning permits were large (Fig. 10a). Our visual inspection using the NASA Worldview tool shows cloud cover was dominated during these days, particularly on February 24. This suggests that cloud obscuration is a significant uncertainty source in satellite fire detections, even for very high-temporal resolution sensors like ABI, in areas where cloud cover is very frequent, as indicated by other studies (Schroeder et al., 2008).

5.2. The GOES-16 ABI Fire Radiative Power (FRP)

The ABI FRP estimate is relatively overestimated in individual fire clusters compared with the 750-m VIIRS FRP estimates. In the selected 211 fire clusters, the ABI fire-cluster FRP is overall ~40% larger than the 750-m VIIRS fire-cluster FRP (Fig. 14). This result contrasts with the previous finding that fire-cluster FRP estimates from geostationary sensors (e.g., SEVIRI, previous GOES, and AHI) are generally comparable with FRP from polar-orbiting sensors (e.g., MODIS) (Roberts and Wooster, 2008; Roberts et al., 2015; Schroeder et al., 2010; Xu et al., 2017), but the geostationary FRP tends to be overestimated in small fires (Roberts and Wooster, 2008; Roberts et al., 2015; Schroeder et al., 2010; Xu et al., 2017). This discrepancy is likely due to uncertainty in background characterization and the consideration of duplicate fire detections of the MODIS sensor at off-nadir view angles. First, to characterize the average radiance of non-fire background pixels for FRP calculation, the context-based ABI and 750-m VIIRS fire detection algorithms search non-fire background pixels that are ~2 km for ABI and ~750 m for VIIRS. As a result, the selected ABI and VIIRS background pixels could consist of significantly different land covers for the same fire, which add uncertainty to pixel-level and fire-cluster FRP estimates, especially for the 2-km ABI sensor. This background effect has been noticed in previous studies (Roberts and Wooster, 2008; Schroeder et al., 2010) and discussed in details (Wooster et al., 2005). Second, the comparison between MODIS and geostationary satellite FRP estimates in previous studies did not consider the uncertainty in fire-cluster MODIS FRP caused by the duplicate fire detections between MODIS adjacent scan lines at off-nadir view angles. The duplicate fire detection is a known issue (Freeborn et al., 2014; Peterson et al., 2013), which could significantly result in the overestimates of fire-cluster FRP (Li et al., 2018). Therefore, we believe our study with the removal of the duplicate fire detections could provide more reliable fire-cluster FRP comparison. Additionally, attenuation of the 750-m VIIRS FRP by fire smoke plumes could add uncertainty to the fire cluster-FRP (Giglio et al., 2016a), but this uncertainty is very limited because the 750-m VIIRS and 1-km MODIS fire-cluster FRP estimates are overall comparable in the southeastern CONUS (Li et al., 2018).

At a regional scale, ABI FRP, however, is comparable with 750-m VIIRS FRP (Fig. 15). Theoretically, we expected that 750-m VIIRS FRP would be larger than 2-km ABI FRP at a regional scale because the VIIRS with finer spatial resolution is able to detect many smaller and cooler fires (e.g., fires with FRP < 34.5 MW), as suggested in the ABI and VIIRS FRP-frequency comparison (Fig. 13). The contribution of these smaller and cooler fires to 750-m VIIRS FRP is possibly offset by the overestimation of ABI FRP in individual fires and the ABI commission errors. The overall comparable FRP estimates from ABI and VIIRS at a regional scale also contrasts with the previous finding that regional-scale FRP estimates from geostationary sensors are ~30-40% smaller than regional-scale MODIS FRP (Roberts and Wooster, 2008; Roberts et al., 2015; Xu et al., 2010, 2017). The possible impacts are the same as the illustrations for the discrepancy of fire cluster FRP.

6 Conclusions

The ABI sensor onboard the GOES-16 and GOES-17, the first two satellites of GOES-R series, operationally detects fires across the America continents with an unprecedented spatiotemporal resolution, which will improve the detection of small fires and enhance biomass burning emissions estimation (Ichoku et al., 2012; Schmit et al., 2017). In this study, we evaluated the fire detection and FRP estimation capability of the GOES-16 ABI sensor using both the higher spatial resolution satellite active fire data and the ground-based fire records across the prescribed fire dominated southeastern CONUS during the peak burning season from January to April 2018. We found that the overall fire detection performance of the ABI fire detection algorithm was associated with fire size and temporal resolution. The ABI detection probability was higher than 95% as an ABI pixel contained more than 114 contemporaneous (a ±2.5 min window) Landsat-8 (30 m) fire detections or 11 VIIRS (375 m) detections. During a ±8-hour period, the ABI detection probability could be improved by up to 61% and the ABI omission error could be reduced by up to 33% relative to that in a ±2.5 min window. Results of comparing with ground-based fire data indicated that ABI was able to detect 6-22% and 31-42% more prescribed-burning fires than the 375-m and 750-m VIIRS in Georgia and Florida States, respectively, and that ABI missed majority of very small fires that were beyond the fire detection capability of the ABI sensor. The FRP evaluation showed that ABI FRP was relatively overestimated by ~30-50% in individual fire events and was overall comparable with 750 m VIIRS FRP for the whole region of the southeastern CONUS.

The evaluation results of the ABI fire detection and FRP estimation suggest some important implications of the current "provisional" GOES-16 ABI active fire data for fire-monitoring and emission-estimating applications. In the southeast, both the 30m Landsat-8 active fire data and the ground-based burning records indicated that a large number of fires are too small or cool to be detected by the ABI and even by the 375 m VIIRS. Regardless of this, the ABI active fire data outperforms VIIRS active fire data in matching ground-based fire records. Hence, ABI is able to help state agencies effectively monitor moderate-to-large prescribed burnings and wildfires in the southeastern CONUS. As wildfires generally burn very intensely and could last from several days to months in the western CONUS (Abatzoglou et al., 2016; Littell et al., 2009; Schmidt et al., 2002), ABI is likely to perform much better in monitoring fires and provide critical fire information (e.g., near real-time fire progression maps) for fire suppression and evacuation. Furthermore, ABI provides FRP retrievals every five minutes, which enables us to directly estimate fire radiative energy and significantly improve fire emissions estimation for near real-time applications (e.g., air quality forecast). However, ABI still missed a significant number of small fires in the southeastern CONUS that could contribute significantly to the total emissions. Alternatively, emissions from small fires could be estimated by relating the very high-temporal resolution ABI AOD to emissions, as demonstrated with MODIS AOD (Mota and Wooster., 2018; Lu et al., 2019).

Acknowledgements

This research was funded by NOAA contracts NA14NES4320003. We want to thank the Georgia Forestry Commission (GFC) agency and the Florida Forest Service (FFS) for providing prescribed-burning records. We also thank USDA Remote Sensing Applications Center, NASA, and NOAA for providing the Landsat-8, VIIRS, and ABI active fire data. The active fire data used in this study are available at USDA Remote Sensing Applications Center (https://fsapps.nwcg.gov/afm/gisdata.php), NASA LAADS (https://ladsweb.modaps.eosdis.nasa.gov/archive/allData/5000/), and NOAA CLASS (https://www.avl.class.noaa.gov/saa/products/welcome). We thank anonymous reviewers for their comments that improved this manuscript. We also want to thank Holly Nowell for helping us use the Florida prescribed-burning data. The manuscript contents are solely the opinions of the author(s) and do not constitute a statement of policy, decision, or position on behalf of NOAA or the U.S. Government.

References

Abatzoglou, J.T., Williams, A.P., 2016. Impact of anthropogenic climate change on wildfire across western US forests. Proceedings of the National Academy of Sciences, 113, 11770-11775. https://doi.org/10.1073/pnas.1607171113.

Ahmadov, R., Grell, G., James, E., Csiszar, I., Tsidulko, M., Pierce, B., McKeen, S., Benjamin, S., Alexander, C., Pereira, G., Freitas, S., & Goldberg, M., 2017. Using VIIRS fire radiative power data to simulate biomass burning emissions, plume rise and smoke transport in a real-time air quality modeling system. In, 2017 IEEE International Geoscience and Remote Sensing Symposium (IGARSS) (pp. 2806-2808). https://doi.org/10.1109/IGARSS.2017.8127581.

Andela, N., Morton, D.C., Giglio, L., Chen, Y., van der Werf, G.R., Kasibhatla, P.S., DeFries, R.S., Collatz, G.J., Hantson, S., Kloster, S., Bachelet, D., Forrest, M., Lasslop, G., Li, F., Mangeon, S., Melton, J.R., Yue, C., Randerson, J.T., 2017. A human-driven decline in global burned area. Science, 356, 1356-1362. https://doi.org/10.1126/science.aal4108.

Bishop, C., 2006. Pattern Recognition and Machine Learning. New York: Springer-Verlag.

Carlomusto, M., 2018. GOES R SERIES PRODUCT DEFINITION AND USERS’ GUIDE (PUG) V2.0. Availabe: https://www.goes-r.gov/products/docs/PUG-L2+-vol5.pdf, last accessed on 12/3/2018.

Cauchy, A., 1847. Méthode générale pour la résolution des systemes d’équations simultanées. Comp. Rend. Sci. Paris, 25, 536-538.

Congalton, R.G., 1991. A review of assessing the accuracy of classifications of remotely sensed data. Remote Sensing of Environment, 37, 35-46. https://doi.org/10.1016/0034-4257(91)90048-B.

Csiszar, I., Schroeder, W., Giglio, L., Ellicott, E., Vadrevu, K.P., Justice, C.O., Wind, B., 2014. Active fires from the Suomi NPP Visible Infrared Imaging Radiometer Suite: Product status and first evaluation results. Journal of Geophysical Research: Atmospheres, 119, 2013JD020453. https://doi.org/10.1002/2013JD020453.

Csiszar, I., Schroeder, W., Giglio, L., Mikles, V., Tsidulko, M., 2016. The NOAA NDE Active Fire EDR External Users Manual, Version 2.6, Available: https://www.star.nesdis.noaa.gov/jpss/documents/ATBD/ATBD_NDE_AF_v2.6.pdf, last accessed on 12/3/2018.

Csiszar, I.A., Morisette, J.T., Giglio, L., 2006. Validation of active fire detection from moderate-resolution satellite sensors: the MODIS example in northern eurasia. Ieee Transactions on Geoscience and Remote Sensing, 44, 1757-1764. https://doi.org/10.1109/TGRS.2006.875941.

Darmenov, A.S., Silva, A.d., 2015. The Quick Fire Emissions Dataset (QFED): Documentation of versions 2.1, 2.2 and 2.4 Rep. TM–2015–104606. In R.D. Koster (Ed.), Technical Report Series on Global Modeling and Data Assimilation (p. 212): NASA

Dozier, J., 1981. A method for satellite identification of surface temperature fields of subpixel resolution. Remote Sensing of Environment, 11, 221-229. https://doi.org/10.1016/0034-4257(81)90021-3.

Earl, N., Simmonds, I., 2018. Spatial and Temporal Variability and Trends in 2001–2016 Global Fire Activity. Journal of Geophysical Research: Atmospheres, 123, 2524-2536. https://doi.org/10.1002/2017JD027749.

Earl, N., Simmonds, I., Tapper, N., 2015. Weekly cycles of global fires—Associations with religion, wealth and culture, and insights into anthropogenic influences on global climate. Geophysical Research Letters, 42, 9579-9589. https://doi.org/10.1002/2015GL066383.

Fowler, C., Konopik, E., 2007. The History of Fire in the Southern United States. Human Ecology Review, 14, 165-176.

Freeborn, P.H., Wooster, M.J., Roberts, G., 2011. Addressing the spatiotemporal sampling design of MODIS to provide estimates of the fire radiative energy emitted from Africa. Remote Sensing of Environment, 115, 475-489. https://doi.org/10.1016/j.rse.2010.09.017.

Freeborn, P.H., Wooster, M.J., Roberts, G., Malamud, B.D., Xu, W., 2009. Development of a virtual active fire product for Africa through a synthesis of geostationary and polar orbiting satellite data. Remote Sensing of Environment, 113, 1700-1711. https://doi.org/10.1016/j.rse.2009.03.013.

Freeborn, P.H., Wooster, M.J., Roy, D.P., Cochrane, M.A., 2014. Quantification of MODIS fire radiative power (FRP) measurement uncertainty for use in satellite-based active fire characterization and biomass burning estimation. Geophysical Research Letters, 41, 2013GL059086. https://doi.org/10.1002/2013GL059086.

Giglio, L., 2007. Characterization of the tropical diurnal fire cycle using VIRS and MODIS observations. Remote Sensing of Environment, 108, 407-421. https://doi.org/10.1016/j.rse.2006.11.018.

Giglio, L., Csiszar, I., Justice, C.O., 2006. Global distribution and seasonality of active fires as observed with the Terra and Aqua Moderate Resolution Imaging Spectroradiometer (MODIS) sensors. Journal of Geophysical Research: Biogeosciences, 111, G02016. https://doi.org/10.1029/2005JG000142.

Giglio, L., Csiszar, I., Restás, Á., Morisette, J.T., Schroeder, W., Morton, D., Justice, C.O., 2008. Active fire detection and characterization with the advanced spaceborne thermal emission and reflection radiometer (ASTER). Remote Sensing of Environment, 112, 3055-3063. https://doi.org/10.1016/j.rse.2008.03.003.

Giglio, L., Descloitres, J., Justice, C.O., Kaufman, Y.J., 2003. An Enhanced Contextual Fire Detection Algorithm for MODIS. Remote Sensing of Environment, 87, 273-282. https://doi.org/10.1016/S0034-4257(03)00184-6.

Giglio, L., Schroeder, W., Csiszar, I., Tsidulko, M., 2016a. Algorithm Theoretical Basis Document For NOAA NDE VIIRS Active Fire, Version 2.6, Available: https://www.star.nesdis.noaa.gov/jpss/documents/ATBD/ATBD_NDE_AF_v2.6.pdf, last accessed on 12/3/2018.

Giglio, L., Schroeder, W., Justice, C.O., 2016b. The collection 6 MODIS active fire detection algorithm and fire products. Remote Sensing of Environment, 178, 31-41. https://doi.org/10.1016/j.rse.2016.02.054.

Hu, X., Yu, C., Tian, D., Ruminski, M., Robertson, K., Waller, L.A., & Liu, Y., 2016. Comparison of the Hazard Mapping System (HMS) fire product to ground-based fire records in Georgia, USA. Journal of Geophysical Research: Atmospheres, 121, 2015JD024448. https://doi.org/10.1002/2015JD024448.

Huang, R., Zhang, X., Chan, D., Kondragunta, S., Russell Armistead, G., Odman, M.T., 2018. Burned Area Comparisons Between Prescribed Burning Permits in Southeastern United States and Two Satellite-Derived Products. Journal of Geophysical Research: Atmospheres, 123, 4746-4757. https://doi.org/10.1029/2017JD028217.

Huff, A.K., Kondragunta, S., Zhang, H., Hoff, R.M., 2015. Monitoring the Impacts of Wildfires on Forest Ecosystems and Public Health in the Exo-Urban Environment Using High-Resolution Satellite Aerosol Products from the Visible Infrared Imaging Radiometer Suite (VIIRS). Environmental Health Insights, 9s2, EHI.S19590. https://doi.org/10.4137/ehi.s19590.

Ichoku, C., Ellison, L., 2014. Global top-down smoke-aerosol emissions estimation using satellite fire radiative power measurements. Atmos. Chem. Phys., 14, 6643-6667. https://doi.org/10.5194/acp-14-6643-2014.

Ichoku, C., Kahn, R., Chin, M., 2012. Satellite contributions to the quantitative characterization of biomass burning for climate modeling. Atmospheric Research, 111, 1-28. https://doi.org/10.1016/j.atmosres.2012.03.007.

Jacobson, M.Z., 2014. Effects of biomass burning on climate, accounting for heat and moisture fluxes, black and brown carbon, and cloud absorption effects. Journal of Geophysical Research: Atmospheres, 119, 2014JD021861. https://doi.org/10.1002/2014JD021861.

Johnston, F.H., Henderson, S.B., Chen, Y., Randerson, J.T., Marlier, M., DeFries, R.S., Kinney, P., Bowman, D.M., Brauer, M., 2012. Estimated global mortality attributable to smoke from landscape fires. Environmental Health Perspectives, 120. https://doi.org/10.1289/ehp.1104422.

Kaiser, J.W., Heil, A., Andreae, M.O., Benedetti, A., Chubarova, N., Jones, L., Morcrette, J.J., Razinger, M., Schultz, M.G., Suttie, M., van der Werf, G.R., 2012. Biomass burning emissions estimated with a global fire assimilation system based on observed fire radiative power. Biogeosciences, 9, 527-554. https://doi.org/10.5194/bg-9-527-2012.

Kennard, D.K., Outcalt, K.W., Jones, D., O'Brien, J.J., 2005. Comparing techniques for estimating flame temperature of prescribed fires. Fire Ecology, 1, 75-84.

Kumar, S.S., & Roy, D.P., 2018. Global operational land imager Landsat-8 reflectance-based active fire detection algorithm. International Journal of Digital Earth, 11, 154-178. https://doi.org/10.1080/17538947.2017.1391341.

Li, F., Zhang, X., Kondragunta, S., Csiszar, I., 2018. Comparison of Fire Radiative Power Estimates From VIIRS and MODIS Observations. Journal of Geophysical Research: Atmospheres, 123, 4545-4563. https://doi.org/10.1029/2017JD027823.

Li, F., Zhang, X., Roy, D.P., & Kondragunta, S., 2019. Estimation of biomass-burning emissions by fusing the fire radiative power retrievals from polar-orbiting and geostationary satellites across the conterminous United States. Atmospheric Environment, 211, 274-287. https://doi.org/10.1016/j.atmosenv.2019.05.017.

Littell, J.S., McKenzie, D., Peterson, D.L., Westerling, A.L., 2009. Climate and wildfire area burned in western U.S. ecoprovinces, 1916–2003. Ecological Applications, 19, 1003-1021. https://doi.org/10.1890/07-1183.1.

Liu, T., Marlier, M.E., DeFries, R.S., Westervelt, D.M., Xia, K.R., Fiore, A.M., Mickley, L.J., Cusworth, D.H., Milly, G., 2018. Seasonal impact of regional outdoor biomass burning on air pollution in three Indian cities: Delhi, Bengaluru, and Pune. Atmospheric Environment, 172, 83-92. https://doi.org/10.1016/j.atmosenv.2017.10.024.

Lu, X., Zhang, X., Li, F., & Cochrane, M.A., 2019. Investigating Smoke Aerosol Emission Coefficients using MODIS Active Fire and Aerosol Products — A Case Study in the CONUS and Indonesia. Journal of Geophysical Research: Biogeosciences, https://doi.org/10.1029/2018jg004974.

Marlier, M.E., DeFries, R.S., Kim, P.S., Koplitz, S.N., Jacob, D.J., Mickley, L.J., Myers, S.S., 2015. Fire emissions and regional air quality impacts from fires in oil palm, timber, and logging concessions in Indonesia. Environmental Research Letters, 10, 085005. https://doi.org/10.1088/1748-9326/10/8/085005.

Mathews, B.J., Strand, E.K., Smith, A.M.S., Hudak, A.T., Hudak, A.T., Dickinson, B., Kremens, R.L., 2016. Laboratory experiments to estimate interception of infrared radiation by tree canopies. International Journal of Wildland Fire, 25, 1009-1014. https://doi.org/10.1071/WF16007.

Melvin, M.A., 2015. 2015 National Prescribed Fire Use Survey Report. In (pp. 1-22): Coalition of Prescribed Fire Councils, Inc. Available: https://stateforesters.org/sites/default/files/publication-documents/2015%20Prescribed%20Fire%20Use%20Survey%20Report.pdf, last accessed on 12/3/2018.

Minnich, R.A., 1983. Fire mosaics in southern California and northern Baja California. Science, 219, 1287-1294. https://doi.org/10.1126/science.219.4590.1287.

Morisette, J.T., Giglio, L., Csiszar, I., Justice, C.O., 2005a. Validation of the MODIS active fire product over Southern Africa with ASTER data. International Journal of Remote Sensing, 26, 4239-4264. https://doi.org/10.1080/01431160500113526.

Morisette, J.T., Giglio, L., Csiszar, I., Setzer, A., Schroeder, W., Morton, D., Justice, C.O., 2005b. Validation of MODIS Active Fire Detection Products Derived from Two Algorithms. Earth Interactions, 9, 1-25. https://doi.org/10.1175/ei141.1.

Mota, B., Wooster, M.J., 2018. A new top-down approach for directly estimating biomass burning emissions and fuel consumption rates and totals from geostationary satellite fire radiative power (FRP). Remote Sensing of Environment, 206, 45-62. https://doi.org/10.1016/j.rse.2017.12.016.

Murphy, S.W., de Souza Filho, C.R., Wright, R., Sabatino, G., Correa Pabon, R., 2016. HOTMAP: Global hot target detection at moderate spatial resolution. Remote Sensing of Environment, 177, 78-88. https://doi.org/10.1016/j.rse.2016.02.027.

Nowell, H.K., Holmes, C.D., Robertson, K., Teske, C., Hiers, J.K., 2018. A New Picture of Fire Extent, Variability, and Drought Interaction in Prescribed Fire Landscapes: Insights From Florida Government Records. Geophysical Research Letters, 45, 7874-7884. https://doi.org/10.1029/2018GL078679.

Peterson, D., Wang, J., Ichoku, C., Hyer, E., Ambrosia, V., 2013. A sub-pixel-based calculation of fire radiative power from MODIS observations: 1: Algorithm development and initial assessment. Remote Sensing of Environment, 129, 262-279. https://doi.org/10.1016/j.rse.2012.10.036.

Prins, E.M., Menzel, W.P., 1994. Trends in South American biomass burning detected with the GOES visible infrared spin scan radiometer atmospheric sounder from 1983 to 1991. Journal of Geophysical Research: Atmospheres, 99, 16719-16735. https://doi.org/10.1029/94JD01208.

Pyne, S.J., Andrews, P.L., Laven, R.D., 1996. Introduction to wildland fire. John Wiley and Sons.

Randerson, J.T., Chen, Y., van der Werf, G.R., Rogers, B.M., Morton, D.C., 2012. Global burned area and biomass burning emissions from small fires. Journal of Geophysical Research: Biogeosciences, 117, G04012. https://doi.org/10.1029/2012JG002128.

Reid, J.S., Hyer, E.J., Prins, E.M., Westphal, D.L., Jianglong, Z., Jun, W., Christopher, S.A., Curtis, C.A., Schmidt, C.C., Eleuterio, D.P., Richardson, K.A., Hoffman, J.P., 2009. Global Monitoring and Forecasting of Biomass-Burning Smoke: Description of and Lessons From the Fire Locating and Modeling of Burning Emissions (FLAMBE) Program. Selected Topics in Applied Earth Observations and Remote Sensing, IEEE Journal of, 2, 144-162. https://doi.org/10.1109/JSTARS.2009.2027443.

Roberts, G., Wooster, M.J., Lagoudakis, E., 2009. Annual and diurnal african biomass burning temporal dynamics. Biogeosciences, 6, 849-866. https://doi.org/10.5194/bg-6-849-2009.

Roberts, G., Wooster, M.J., Lauret, N., Gastellu-Etchegorry, J.P., Lynham, T., McRae, D., 2018. Investigating the impact of overlying vegetation canopy structures on fire radiative power (FRP) retrieval through simulation and measurement. Remote Sensing of Environment, 217, 158-171. https://doi.org/10.1016/j.rse.2018.08.015.

Roberts, G., Wooster, M.J., Xu, W., Freeborn, P.H., Morcrette, J.J., Jones, L., Benedetti, A., Jiangping, H., Fisher, D., Kaiser, J.W., 2015. LSA SAF Meteosat FRP products – Part 2: Evaluation and demonstration for use in the Copernicus Atmosphere Monitoring Service (CAMS). Atmos. Chem. Phys., 15, 13241-13267. https://doi.org/10.5194/acp-15-13241-2015.

Roberts, G.J., Wooster, M.J., 2008. Fire Detection and Fire Characterization Over Africa Using Meteosat SEVIRI. Geoscience and Remote Sensing, IEEE Transactions on, 46, 1200-1218. https://doi.org/10.1109/TGRS.2008.915751.

Roberts, G., Wooster, M.J., Perry, G.L.W., Drake, N., Rebelo, L.M., & Dipotso, F., 2005. Retrieval of biomass combustion rates and totals from fire radiative power observations: Application to southern Africa using geostationary SEVIRI imagery. Journal of Geophysical Research: Atmospheres, 110, D21111. https://doi.org/10.1109/10.1029/2005JD006018.

Rothermel, R.C., 1972. A mathematical model for predicting fire spread in wildland fuels. Res. Pap. INT-115. Ogden, UT: U.S. Department of Agriculture, Intermountain Forest and Range Experiment Station., 40.

Ryan, K.C., Knapp, E.E., Varner, J.M., 2013. Prescribed fire in North American forests and woodlands: history, current practice, and challenges. Frontiers in Ecology and the Environment, 11, e15-e24. https://doi.org/10.1890/120329.

Schmidt, C.C., Hoffman, J., Prins, E., Lindstrom, S., 2012. GOES-R Advanced Baseline Imager (ABI) Algorithm Theoretical Basis Document For Fire / Hot Spot Characterization, Version 2.5, edited, pp. 1-97, NOAA NESDIS STAR.

Schmidt, C.C., Prins, E.M., 2003. GOES wildfire ABBA applications in the western hemisphere. In, 2nd International Wildland Fire Ecology and Fire Management Congress and 5th Symp. on Fire and Forest Meteorology (pp. 16-20).

Schmidt, K.M., Menakis, J.P., Hardy, C.C., Hann, W.J., Bunnell, D.L., 2002. Development of coarse-scale spatial data for wildland fire and fuel management. Gen. Tech. Rep. RMRS-GTR-87. Fort Collins, CO: US Department of Agriculture, Forest Service, Rocky Mountain Research Station. 41 p.+ CD., 87. https://doi.org/10.2737/RMRS-GTR-87.

Schmit, T.J., Griffith, P., Gunshor, M.M., Daniels, J.M., Goodman, S.J., Lebair, W.J., 2017. A Closer Look at the ABI on the GOES-R Series. Bulletin of the American Meteorological Society, 98, 681-698. https://doi.org/10.1175/bams-d-15-00230.1.

Schroeder, W., Csiszar, I., Giglio, L., Schmidt, C.C., 2010. On the use of fire radiative power, area, and temperature estimates to characterize biomass burning via moderate to coarse spatial resolution remote sensing data in the Brazilian Amazon. Journal of Geophysical Research: Atmospheres, 115, D21121. https://doi.org/10.1029/2009JD013769.

Schroeder, W., Giglio, L., 2017. NASA SPIS 375 m 750 m Active Fire Detection Product User's Guide, Version 1.3, Available: https://lpdaac.usgs.gov/sites/default/files/public/product_documentation/vnp14_user_guide_v1.3.pdf, last accessed on 12/3/2018.

Schroeder, W., Oliva, P., Giglio, L., Csiszar, I.A., 2014. The New VIIRS 375 m active fire detection data product: Algorithm description and initial assessment. Remote Sensing of Environment, 143, 85-96. https://doi.org/10.1016/j.rse.2013.12.008.

Schroeder, W., Oliva, P., Giglio, L., Quayle, B., Lorenz, E., Morelli, F., 2016. Active fire detection using Landsat-8/OLI data. Remote Sensing of Environment, 185, 210-220. https://doi.org/10.1016/j.rse.2015.08.032.

Schroeder, W., Prins, E., Giglio, L., Csiszar, I., Schmidt, C., Morisette, J., Morton, D., 2008. Validation of GOES and MODIS active fire detection products using ASTER and ETM+ data. Remote Sensing of Environment, 112, 2711-2726. https://doi.org/10.1016/j.rse.2008.01.005.

Smith, R.J., 2009. Use and misuse of the reduced major axis for line-fitting. American Journal of Physical Anthropology, 140, 476-486. https://doi.org/10.1002/ajpa.21090.

Tian, D., Wang, Y., Bergin, M., Hu, Y., Liu, Y., Russell, A.G., 2008. Air Quality Impacts from Prescribed Forest Fires under Different Management Practices. Environmental Science Technology, 42, 2767-2772. https://doi.org/10.1021/es0711213.

Vadrevu, K., & Lasko, K., 2018. Intercomparison of MODIS AQUA and VIIRS I-Band Fires and Emissions in an Agricultural Landscape—Implications for Air Pollution Research. Remote Sensing, 10, 978. https://doi.org/10.3390/rs10070978.

van der Werf, G.R., Randerson, J.T., Giglio, L., van Leeuwen, T.T., Chen, Y., Rogers, B.M., Mu, M., van Marle, M.J.E., Morton, D.C., Collatz, G.J., Yokelson, R.J., Kasibhatla, P.S., 2017. Global fire emissions estimates during 1997–2016. Earth Syst. Sci. Data, 9, 697-720. https://doi.org/10.5194/essd-9-697-2017.

Wang, J., Bhattacharjee, P.S., Tallapragada, V., Lu, C.H., Kondragunta, S., da Silva, A., Zhang, X., Chen, S.P., Wei, S.W., Darmenov, A.S., McQueen, J., Lee, P., Koner, P., Harris, A., 2018. The implementation of NEMS GFS Aerosol Component (NGAC) Version 2.0 for global multispecies forecasting at NOAA/NCEP – Part 1: Model descriptions. Geosci. Model Dev., 11, 2315-2332. https://doi.org/10.5194/gmd-11-2315-2018.

Wiedinmyer, C., Quayle, B., Geron, C., Belote, A., McKenzie, D., Zhang, X., O'Neill, S., Wynne, K.K., 2006. Estimating emissions from fires in North America for air quality modeling. Atmospheric Environment, 40, 3419-3432. https://doi.org/10.1016/j.atmosenv.2006.02.010.

Wooster, M.J., Roberts, G., Perry, G.L.W., Kaufman, Y.J., 2005. Retrieval of biomass combustion rates and totals from fire radiative power observations: FRP derivation and calibration relationships between biomass consumption and fire radiative energy release.

Journal of Geophysical Research-Atmospheres, 110, D24311. https://doi.org/10.1029/2005jd006318.

Wooster, M.J., Zhukov, B., Oertel, D., 2003. Fire radiative energy for quantitative study of biomass burning: derivation from the BIRD experimental satellite and comparison to MODIS fire products. Remote Sensing of Environment, 86, 83-107. https://doi.org/10.1016/S0034-4257(03)00070-1.

Xu, W., Wooster, M.J., Kaneko, T., He, J., Zhang, T., Fisher, D., 2017. Major advances in geostationary fire radiative power (FRP) retrieval over Asia and Australia stemming from use of Himarawi-8 AHI. Remote Sensing of Environment, 193, 138-149. https://doi.org/10.1016/j.rse.2017.02.024.

Xu, W., Wooster, M.J., Roberts, G., Freeborn, P., 2010. New GOES imager algorithms for cloud and active fire detection and fire radiative power assessment across North, South and Central America. Remote Sensing of Environment, 114, 1876-1895. https://doi.org/10.1016/j.rse.2010.03.012.

Yang, E.-S., Christopher, S.A., Kondragunta, S., Zhang, X., 2011. Use of hourly Geostationary Operational Environmental Satellite (GOES) fire emissions in a Community Multiscale Air Quality (CMAQ) model for improving surface particulate matter predictions. Journal of Geophysical Research: Atmospheres, 116, JD014482. https://doi.org/10.1029/2010JD014482.

Zeng, T., Wang, Y., Yoshida, Y., Tian, D., Russell, A.G., Barnard, W.R., 2008. Impacts of Prescribed Fires on Air Quality over the Southeastern United States in Spring Based on Modeling and Ground/Satellite Measurements. Environmental Science Technology, 42, 8401-8406. https://doi.org/10.1021/es800363d.

Zhang, T., Wooster, M.J., & Xu, W., 2017a. Approaches for synergistically exploiting VIIRS I- and M-Band data in regional active fire detection and FRP assessment: A demonstration with respect to agricultural residue burning in Eastern China. Remote Sensing of Environment, 198, 407-424. http://dx.doi.org/10.1016/j.rse.2017.06.028.

Zhang, X., Hecobian, A., Zheng, M., Frank, N.H., Weber, R.J., 2010. Biomass burning impact on PM2.5 over the southeastern US during 2007: integrating chemically speciated FRM filter measurements, MODIS fire counts and PMF analysis. Atmos. Chem. Phys., 10, 6839-6853. https://doi.org/10.5194/acp-10-6839-2010.

Zhang, X., Kondragunta, S., Da Silva, A., Lu, S., Ding, H., Li, F., & Zhu, Y., 2017b. The Blended Global Biomass Burning Emissions Product from MODIS, VIIRS, and Geostaionary Satellites (GBBEPx) Version 2.0. In: NOAA/NESDIS/STAR, available at https://www.ospo.noaa.gov/Products/land/gbbepx/docs/GBBEPx_ATBD.pdf, last access on 10/8/2019.

Zhang, X., Kondragunta, S., Ram, J., Schmidt, C., Huang, H.-C., 2012. Near-real-time global biomass burning emissions product from geostationary satellite constellation. Journal of Geophysical Research-Atmospheres, 117, D14201. https://doi.org/10.1029/2012jd017459.

Zhang, X., Kondragunta, S., Roy, D.P., 2014. Interannual variation in biomass burning and fire seasonality derived from geostationary satellite data across the contiguous United States from 1995 to 2011. Journal of Geophysical Research: Biogeosciences, 119, JG002518. https://doi.org/10.1002/2013JG002518.

List of Figure Captions

Fig. 1. Relative spectral response functions of the fire-detecting middle-infrared bands of GOES-16 ABI (channel7 at ~3.71-4.09µm) and Suomi NPP VIIRS (I4 at ~3.47-4.03µm and M13 at ~3.89-4.24µm). The ABI and VIIRS relative spectral response functions were obtained from NOAA National Calibration Center (https://ncc.nesdis.noaa.gov/index.php).

Fig. 2. GOES-16 ABI view zenith angle (a) and pixel area (b) across the southeastern CONUS.

Fig. 3. Distributions of 56 Landsat-8 scenes (a) and active fire detections across the southeastern CONUS between January and April 2018 from USDA (b) and from both USDA and this study (additional 92 scenes) (c).

Fig. 4. Flowchart of modeling the ABI fire detection probability using the contemporaneous Landsat-8 and 375-m VIIRS active fire detections.

Fig. 5. Extraction of contemporaneous fire clusters. (a) shows an example of manually extracting fire clusters using the contemporaneous ABI and 750-m VIIRS fire detections collected at ~18:10 (UTC) on 03/02/2018. The square-shape image zooms in an extracted fire cluster highlighted using magenta circle in the map. (b) shows the distribution of the extracted 211 fire clusters across the southeastern CONUS.

Fig. 6. The ABI fire detection probability modeled using fire pixels detected contemporaneously by ABI and Landsat-8. (a-b) show histograms of the count of the 30-m Landsat-8 fire pixels within a 2-km ABI pixel that was detected as either an ABI fire pixel or a non-fire pixel within ±2.5 min of the Landsat-8 observing time. (c-d) display the same information as (a-b) but for an 8 hr observing time difference. (e) shows the ABI fire detection probability within a temporal window of the ±2.5 min (red line) and ±8 hr (blue line), respectively.

Fig. 7. The ABI fire detection probability modeled using fire pixels detected contemporaneously by 2 km ABI and 375 m VIIRS. (a-e) show the same information as (Fig. 4a-e) but for the 375-m VIIRS fire pixels.

Fig. 8. Variations of the omission error probability of the ABI fire detections. The probability of omission errors estimated by comparing with the contemporaneous 30-m Landsat-8 fire detections (a, c, e, and g) and 375-m VIIRS fire detections (b, d, f, and h). The omission error probability varying with ABI fire detection categories: group 1 (a-b), groups 1-2 (c-d), groups 1-3 (e-f), and groups 1-4 (g-h).

Fig. 9. ABI fire detections spatially matched and not matched (false alarms) with the 375-m VIIRS fire detection within ±2.5 min of VIIRS daytime overpasses in the selected 25 days across the southeastern CONUS. (a) Matched ABI fire detections. (b-e) Not-matched ABI fire detections for group 1 (b), group 2 (c), group 3 (d), and group 4 (e). In (b-e), pink dots show ABI false alarms that occurred in the same locations where both ABI and VIIRS

detected fires in previous days or occurred in the adjacent pixels of these locations, and blue dots indicate ABI false alarms that were far away from these locations.

Fig. 10. Daily count of the prescribed-burning permits and satellite active fire detections in Georgia (a) and Florida (b) States from January-April 2018.

Fig. 11. The satellite active fire detections spatially matched with the prescribed-burning permits in Georgia State during the selected 25 days. (a) The number of geolocated prescribed-burning permits varying with the planned start and end burning times. (b) The diurnal profile of ABI fire detections characterized by hourly mean detection count. (c) The percent of prescribed-burning permits spatially matched with satellite active fire detections, varying with the planed begin burning times. (d), (e), and (f) are the percent of burning permits in five groups stratified by size of area planned to burn, with geolocations in each group, and spatially matched with satellite active fire detections in each group, respectively. Note the terms “2.5min” and “day” in legend represent GOES-16 ABI fire detections observed within ±2.5min of VIIRS overpass time and during all day, respectively.

Fig. 12. The prescribed-burning permits spatially matched by GOES-16 ABI and VIIRS 375m and 750m active fire detections in Florida State during the selected 25 days. The percent of the spatially matched burning permits varying with five-stratified groups of area size planned to burn: (a) for all purposes (silvicultural, agricultural, and land clearing) , (b) for silvicultural purpose, (c) for agricultural purpose. Note the terms “2.5min” and “day” in legend are the same as in Fig. 11.

Fig. 13. Frequency density of the contemporaneous ABI and 750-m VIIRS pixel-level FRP. The red and blue dashed vertical lines respectively show the occurrences of the maximum frequency density at FRP bins of the ABI (34.5 MW) and 750 m VIIRS (7.1 MW).

Fig. 14. Comparison of the contemporaneous ABI and 750-m VIIRS FRP estimates in the selected 211 fire clusters. The fire clusters were sensed by the two sensors within a ±2.5 min observing time difference and are colored by ABI view zenith angle ranging from 30° to 44°. The black solid line is the best-fitted line and the black dashed lines show the lower and upper bound of the fitted line in a 95% confidence interval (CI). For the best-fitted model, the values after "±" are the 95% CIs of the constant and slope coefficients whose p-values are the $p_{constant}$ and p_{slope}, respectively.

Fig. 15. Comparison of the contemporaneous ABI and 750-m VIIRS FRP estimates in the southeastern CONUS region during the selected 25 significant burning days. Each sample (filled circle) represents the daily cumulative FRP estimates of the fire detections contemporaneously observed by ABI and VIIRS within ±2.5 min and is colored with observing day of year (DOY). The black solid line is the best-fitted line and the black dashed lines show the lower and upper bound of the fitted line in a 95% confidence interval (CI). For the best-fitted model, the values after "±" are the 95% CIs of the constant and slope coefficients whose p-values are the $p_{constant}$ and p_{slope}, respectively.